ADVANCED MATERIALS
www.advmat.de

Ionic Conduction-Based Polycrystalline Oxide Gamma Ray Detection – Radiation-Ionic Effects

Thomas Defferriere, Ahmed Sami Helal, Ju Li,* Jennifer L. M. Rupp,* and Harry L. Tuller**

Newly discovered opto-ionic effects in metal oxides provide unique opportunities for functional ceramic applications. The authors generalize the recently demonstrated grain boundary opto-ionic effect observed in solid electrolyte thin films under ultraviolet (UV) irradiation to a radiation-ionic effect that can be applied to bulk materials and used for gamma-rays (γ-rays) detection. Near room temperature, lightly doped Gd-doped CeO_2, a polycrystalline ion conducting ceramic, exhibits a resistance ratio change $\approx 10^3$ and reversible response in ionic current when exposed to ^{60}Co γ-ray (1.1 and 1.3 MeV). This is attributed to the steady state passivation of space charge barriers at grain boundaries, that act as virtual electrodes, capturing radiation-induced electrons, in turn lowering space charge barrier heights, and thereby exclusively modulating the ionic carrier flow within the ceramic electrolytes. Such behavior allows significant electrical response under low fields, that is, < 2 V cm^{-1}, paving the way to inexpensive, sensitive, low-power, and miniaturizable solid-state devices, uniquely suited for operating in harsh (high temperature, pressure, and corrosive) environments. This discovery presents opportunities for portable and/or scalable radiation detectors benefiting geothermal drilling, small modular reactors, nuclear security, and waste management.

1. Introduction

High-performance, low-cost nuclear radiation detectors based on semiconductors have broad applicability in homeland security (nonproliferation of nuclear materials), industrial and medical imaging, nuclear energy, radioactive waste monitoring, oil/gas/geothermal exploration, and fundamental scientific research. While state-of-the-art semiconducting nuclear radiation sensing technologies can achieve high performance, they remain either costly, for example, CdZnTe, or inconvenient (e.g., cryogenic cooling required for high purity germanium, HPGe) for widespread use as portable or large-area device monitors. Furthermore, the detrimental impact of lattice defects on semiconducting performance requires complex crystal growth processing to achieve high-quality materials and, thereby, high sensing efficiency that relies on large electronic carrier mobility-lifetime ($\mu\tau$) products. The search for alternative defect-insensitive, highly effective atomic number (i.e., high-Z), and wide-bandgap material candidates that can be produced with large areas and that are chemically, thermally, and mechanically robust has remained commercially elusive. Materials such as $CsPbBr_3$, TlBr, $FAPbBr_3/MAPbBr_3$, $MAPbI_3$, and $TlInSe_2$ have shown promising radiation monitoring properties, but proofs of concepts to date still require single crystal, limiting scalability.[1,2] Moreover, they suffer from a variety of environmental and operational degradation mechanisms

T. Defferriere, J. Li, J. L. M. Rupp, H. L. Tuller
Department of Material Science and Engineering
MIT
Cambridge, MA 02139, USA
E-mail: tdefferr@mit.edu; liju@mit.edu; tuller@mit.edu
A. S. Helal, J. Li
Department of Nuclear Science and Engineering
MIT
Cambridge, MA 02139, USA
A. S. Helal
Nuclear Materials Authority
Katameya, 3rd Settlement, Cairo 11936, Egypt
J. L. M. Rupp
Department of Chemistry
Technical University Munich
85748 Garching, Germany
J. L. M. Rupp
Department of Electrical Engineering and Computer Science
MIT
Cambridge, MA 02139, USA
J. L. M. Rupp
TUMint. Energy Research GmbH, Lichtenbergstr. 4
85747 Garching, Germany
E-mail: jrupp@tum.de

The ORCID identification number(s) for the author(s) of this article can be found under https://doi.org/10.1002/adma.202309253

DOI: 10.1002/adma.202309253

related to ionic defect migration under applied direct current (DC) potential, resulting in undesirable and irreversible electrochemical reactions at the electrodes[3–6] that alter the charge transfer and collection efficiency of semiconductor-based sensing devices, ultimately complicating the overall device design and operation.

In applications involving γ-rays, oxide ceramics have typically been employed as electrical insulators in core reactor circuits, host matrices for nuclear fuels, or radioactive waste encapsulation, considering their structural and insulating properties. Their refractory nature and chemical inertness allow them to withstand extreme conditions such as high temperatures, while their open and stable crystalline structures lead to enhanced resistance to radiation damage.[7–9] However, to our knowledge, oxide materials have rarely been employed directly as voltage-biased "semiconductor" radiation detectors and have more often been used for their scintillation properties. This originates from their structural and chemical properties (high volumetric mass density, high effective atomic number Z, good optical transparency, adjustable host composition, and flexible doping), enabling rapid electronic charge carrier recombination kinetics and leading to high light output efficiency.[10,11] Regarding semiconducting detection schemes, some studies on ZnO[12] and Ga_2O_3[13] have been conducted, as they exhibit some of the highest electron mobilities in wide band gap oxide systems, but these have typically achieved poor performances due to short electronic carrier recombination lifetimes. Considering the high ionic defect concentrations commonly found in metal oxides, typically leading to electronic charge carrier trapping, it is understandable that poor detection performance would be expected in the semiconducting detection mode, where the aim is to efficiently collect generated electron/hole pairs at the electrodes. While these high ionic defect concentrations are undesirable for electronic semiconducting applications, they are essential in designing electrochemical-based energy conversion devices that are based on ionic conduction. Such high ionic defect concentrations in oxides are critical to supporting fast ionic conduction (with ionic contribution to the electrical conductivity on the order of S/m which is comparable to the electrical conductivity of lightly doped silicon), forming the basis of solid electrolytes vital for applications ranging from batteries, solid oxide fuel cells and electrolyzers, oxygen gas sensors, and permeation membranes.[14–16] To date, few studies have investigated how irradiation impacts ionic transport in purely ion-conducting solid electrolytes, and when they have been pursued, they have typically been focused on irreversible degradation induced within the oxide structures,[8,7,17,18] rather than as a novel radiation detection mechanism. Given the large effective masses of ions and exceptionally low carrier mobilities, polycrystalline oxides have, therefore, not been seriously considered radiation detectors to date.

This study aims to test how the modulation of grain boundary space charge barriers by γ-ray irradiation in polycrystalline oxide-based solid electrolytes could serve as a new design principle for direct radiation detection in solid electrolytes by ionic conduction. If successful, this would provide great promise in moving away from costly electronically conducting materials and, instead, enable the design of inexpensive, robust, and scalable radiation detectors based on polycrystalline ceramics that could operate under extreme environments, that is, at high temperatures and pressures and/or under corrosive environments. Such detection schemes could be expected to have a significant impact on the development and operation of next-generation nuclear clean energy solutions. This encompasses, for example, deep geothermal directional drilling technologies, where in situ identification and quantification of radioactive pockets deeper in the earth's crust is essential, and where high temperature and pressure operation is essential. Likewise, the safe development, operation, and management of third- and fourth-generation nuclear power plants require the use of nuclear detection instrumentation to monitor neutron fluxes that presently utilize bulky, high-voltage boron-lined ionization chambers.[19] The ability to move towards low voltage, miniturizable solid-state systems that can distinguish between neutrons and gamma rays and operate with high dynamic range, while also being able to sustain harsh environments, would be a critical component of designing high-temperature small modular reactors (SMR). Finally, the need for large-area detectors for security & radioactive waste management would further benefit from the ability to scale such detectors into large and inexpensive polycrystalline ceramic panels.

In this study, we show for the first time how γ-ray exposure can modulate the ionic conductivity of a polycrystalline bulk solid electrolyte ceramic. This phenomenon takes advantage of our recent discovery where we demonstrated a similar effect in thin film samples of three at% Gd doped CeO_2 (3GDC) under ultraviolet (UV) irradiation.[20] Here, one takes advantage of the fact that space charge barriers that form at grain boundaries in 3GDC act as barriers to the flow of ions between adjacent grains, leading to many orders of magnitude increases in the overall ionic resistivity.[21,22] We described how field-assisted photogenerated charge separation by built-in electric fields within the space charge zone leads to subsequent trapping of the photogenerated electronic carriers at the grain boundaries. These trapped carriers serve to passivate the grain boundary (GB) core charge, thereby lowering the barriers to the flow of ions. These findings are analogous to reports made for polycrystalline semiconductors such as silicon[23] and III–V semiconductor compounds such as GaAs.[24,25] Theoretical considerations by Seager and Bhatt and Joshi,[26] among others, describe how photogenerated charges screen the space charge potential existing at GBs due to dissimilar trapping of minority and majority charge carriers. However, a key difference is that our majority charge carrier is a mobile ionic defect.

While having demonstrated the opto-ionic concept, the effective penetration depth of our UV radiation of ≈200 nm limited our studies to thin film geometries. Taking advantage of the much larger penetration depths of high-energy ionizing radiation (e.g., mm, for example, in the case of high energy γ-rays), we demonstrate a large and reversible sensing response to ^{60}Co γ-Ray (1.1 and 1.3 MeV) in a bulk polycrystalline 3GDC pellet, an oxygen ion conducting solid electrolyte. This measured "radio-ionic effect" under penetrating gamma irradiation is demonstrated to be exclusively associated with grain boundary resistance modulation over a broad temperature range of up to 300 °C. 3GDC was selected as our model material due to its non-toxicity, chemical inertness, thermal stability, and biocompatibility, making it much easier to handle than alternative potentially toxic Cd- or Pb-based halide material counterparts.

Furthermore, while our materials exhibit a high bulk oxygen ionic conductivity,[7,17] we take advantage of the fact that 3GDC suffers from high grain boundary resistance at lower dopant levels (<5 at%) due to the space charge depletion of oxygen vacancies.[27,28] The detailed physics associated with bulk and grain boundary ionic transport in polycrystalline ionic conductors have been previously described,[20,29,30] but we summarize key features in the supplement for the benefit of the reader (see Sections S1 and S2, Supporting Information). Additionally, 3GDC's bandgap energy of just over 3 eV, high Z (≈60), and large bulk ionic migration energy (≈0.7 eV) allow for a very high ambient dark resistance, all the while offering high radiation-stopping power, thereby enabling efficient absorption of radiation.

Structural deformation, amorphization, and different defect states are commonly generated in crystalline detector materials upon exposure to hard radiation leading to potential instabilities.[22,31] This can lead to leakage charge currents through the formation of defects and subsequent mechanical failure due to induced swelling. In the context of ceramics, for example, reports indicate that this type of damage can strongly depend on the magnitude of the applied voltage in, for example, Al_2O_3 which is commonly used as a barrier coating in nuclear reactor and waste management components.[18,32–34] Considering that during radiation detection, we only attempt to measure the overall linear ionic resistance of our systems, without trying to capture the photogenerated electronic charge carriers, we do not utilize high-bias voltages. Indeed, we show that we can record large resistance modulations using a sinusoidal driving voltage of only ±200 mV, leading to electric field strengths < 2 V cm^{-1}. We furthermore show through combined ex situ long-range XRD and short-range Raman measurements, that our material, intentionally doped with a fixed valent element (i.e., Gd^{3+}) to introduce ionic lattice defects and suppress the formation of Ce^{3+}, exhibits strong resistance to irradiation-induced defect formation and good structural stability even under large γ-ray doses up to ≈1MGy.

Finally, considering that GBs in our solid electrolyte act as virtual electrodes to collect the photogenerated electronic charge carriers on the sub-micron scale, we will discuss how the physics of grain boundary recombination can impact our ionic device responses. Altogether, this work demonstrates the viability of using ion-conducting solid electrolyte materials for radiation detection purposes and lays the groundwork for developing future criteria that can aid in exploring alternative radio-ionic material systems and device design options for gamma radiation detectors.

2. Results

2.1. Structure Analysis

We fabricated a 1-inch diameter by 800-micron thick pellet of 3GDC (labeled A) according to the procedures outlined in the experimental section. To maintain a relatively large grain boundary density, we limited the sintering temperature to 1300 °C for 8 h, yielding a relative theoretical density of 92% and an average grain size of ≈400 nm (see Section S3, Supporting Information for SEM, XRD, Raman, and SEM of the as-prepared sample). The sample was cut in two so that one half was used in the in situ radiation conductivity studies, while the other half was used for chemical and structural analysis. We next discuss the results of ex situ long-range and short-range structural measurements (XRD and Raman) performed to confirm the overall structural and chemical stability of our 3GDC specimens under γ-ray exposure.

To further demonstrate the stability of our specimen under high irradiation dose, we prepared two additional pellets of 3GDC (labeled B and C) that were sintered as bars and cut into three identically shaped pieces with a cross-section of 5 × 5 mm. One piece of each sample was kept as a reference for the "non-irradiated" condition, while the other pieces were placed inside glass test tubes sealed with a cork and exposed to 500 kGy and 1MGy doses, respectively. This was achieved by placing them in a Gammacell 220 irradiator at room temperature for durations of 15 and 30 days, respectively. After exposure, all samples were collected and their XRD and Raman spectra were measured. Images of all samples, and details of their geometries, are provided in Figures S5 and S6 and Table S1, Supporting Information.

In **Figure 1** we display the XRD results for one of the two bulk specimens (B, while results for C are presented in Section S4, Supporting Information) for the various irradiation doses (no exposure, 500 kGy, 1 MGy). From the top spectra, we can see that the same peaks are present for all three samples, similar to the pristine sample (displayed in Figure S4, Supporting Information), at the same positions, demonstrating good phase purity of the face-centered cubic structure of CeO_2. In Section S4, Supporting Information, we also provide the results of the Rietveld fits for both B and C samples that show good agreement with GDC reference patterns and consistent agreements with each other when comparing spectra obtained for the various irradiation doses. **Table 1** below summarizes the lattice constant, lattice volume, March/Dollase, and atomic site occupancies obtained from the fits for the pristine in situ sample and sample B (in Section S4, Supporting Information, results are also reported for samples from series C in Table S1, Supporting Information).

We find that the samples exhibit a slightly preferred crystal orientation (texture), with a March/Dollase factor < 1 indicative of plate-like morphologies. This preferential orientation is found in all three sets of samples (pristine in situ samples, B and C). Moreover, the SEM images in supplementary III for the pristine in situ sample reveal no visible orientation indications for these microstructures. GDC sintered by conventional means are known to show a (111) over (200) orientation preference,[35] indicating this could be an artifact of the powder preparation introduced due to preferential alignment during uniaxial pressing. Next, in the bottom spectra of Figure 1, examining a magnification of superimposed (111) and (200) peaks for all three samples, one finds that the peaks perfectly overlap, both in position and width. In Section S4, Supporting Information, we also provide an unnormalized data set for samples from series B and C, with a magnification of the background for all three samples. These observations support the conclusion that no measurable structural degradation was induced during irradiation (i.e., amorphization, changes related to strain, or changes in grain size or orientation). Unfortunately, due to preferential orientation in the sintered pellets, we could not accurately evaluate the occupancy of the oxygen sublattice,

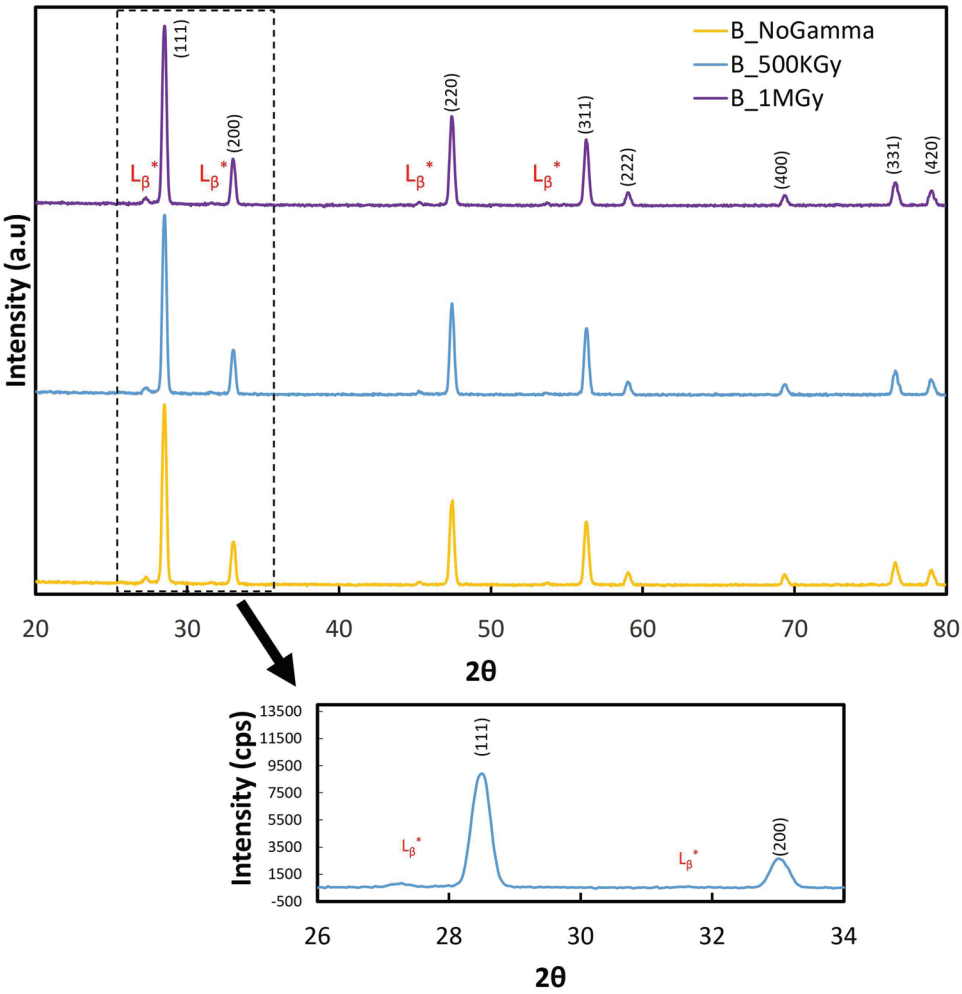

Figure 1. (Top) Normalized and cascaded view of XRD spectra for bulk samples of 3GDC series B, each exposed to various irradiation doses (0, 500 kGy, 1 MGy). (Bottom) Un-normalized magnification of superimposed (111) and (200) peaks for all three samples.

which would be associated with changes in the oxidation state of the Ce ion. Raman spectroscopy, which can probe the symmetric breathing mode of the oxygen octahedra surrounding the host Ce cation, fortunately, can be used to identify changes in either of those properties.

In **Figure** 2a, we display the Raman spectra for the additional 3GDC bulk samples that were prepared and exposed analogous to the XRD section to various radiation doses (no exposure, 500 kGy, 1 MGy). Compared to the Raman spectrum of the sample presented in Figure S4, Supporting Information, all the same key Raman features are present: F_{2g} (464.61 cm^{-1}), and defect bands (550 and 600 cm^{-1}), confirming the similarities in sample chemistry. One can see that exposure to γ-rays had no visible impact on any of these bands, with no evidence for the appearance of secondary phases. A closer zoom-in on the F_{2g} peak in Figure 2b reveals no apparent peak shift in the F_{2g} (464.61 cm^{-1})

Table 1. Structural parameters for the pristine in situ sample and GDC sample B series for various γ irradiation conditions.

Parameters	Pristine in situ sample	0 kGy	500 kGy	1000 kGy
Lattice constants Å, $a = b = c$	5.412	5.412	5.412	5.412
Volume [Å]^3	158.516	158.516	158.516	158.516
March/Dollase (preferred orientation)	0.89	0.81	0.85	0.84
		Occupancy		
Ce	0.970	0.970	0.972	0.970
Gd	0.0299	0.0300	0.0285	0.0299

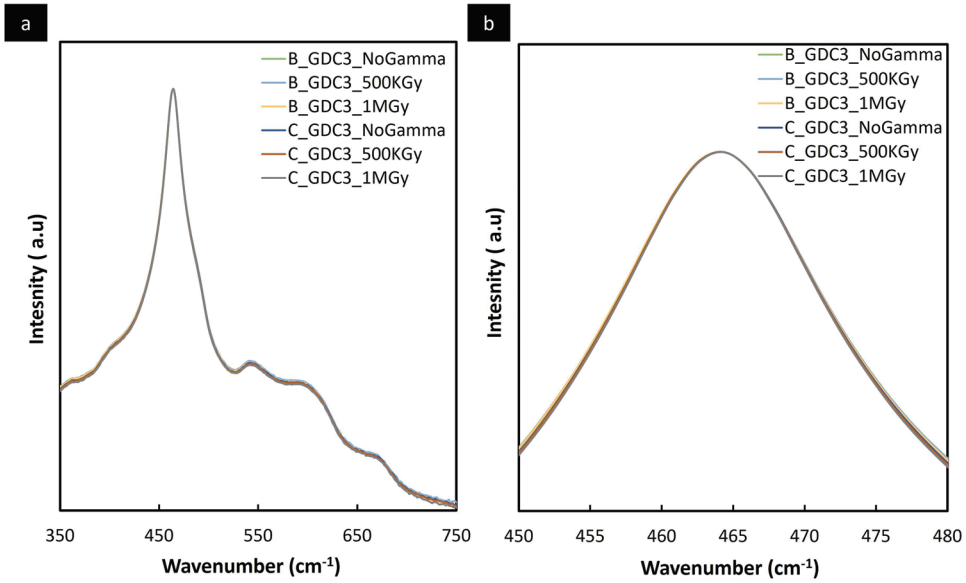

Figure 2. Raman spectra with 473 nm wavelength for two bulk samples of 3GDC (B and C) cut into three pieces and each exposed to various irradiation doses (0, 500 kGy, 1 MGy). a) Complete spectra with main F_{2g} peak (465 cm^{-1}) and defect bands (550 and 600 cm^{-1}); b) magnification of F_{2g} peak for different radiation doses.

vibrational mode, consistent with no change in the oxidation state of Ce under irradiation. An important secondary finding is that the oxygen non-stoichiometry and defect-related Raman modes show no indication of any alterations towards γ-rays within error, these modes being very sensitive to changes in intrinsic or extrinsic defects.[36]

These observations allow us to conclude that gamma irradiation at room temperature has no apparent long-term impact on the chemistry or structure of the material, especially as they relate to changes in defect concentration, grain size, crystallinity degree, or local lattice microstrain due to changes in cation oxidation state. While it is possible that some reduction of Ce^{4+} to Ce^{3+} occurs during irradiation, since there is no evidence for this from the Raman studies, the sample would have had to reoxidize rather rapidly upon removal of the irradiator, even at room temperature. We thereby conclude that 3 at% Gd doped CeO_2 is not only an interesting choice for demonstration of an opto-ionic effect but is also an excellent candidate for demonstrating gamma-ray driven radio-ionic effect and radiation detectors, given its stability and ease of handling for sensing device architectures.

2.2. Electrical Characterization

Electrochemical impedance measurements were performed on 3GDC polycrystalline pellets onto which 5 × 9 mm platinum electrodes were deposited on either side by DC sputtering. To establish a reference value for the electrical conductivity in the dark, we characterized the impedance from 100 to 300 °C to aid in isolating the grain and grain boundary resistance contributions. A typical impedance spectrum measured at 141.7 °C is displayed in **Figure** 3a, and the equivalent circuit used to extract key impedance parameters is given in Figure 3b. As constant phase elements (CPE) were used instead of capacitance, capacitance values were calculated from $C = (R^{1-n}Q)^{\frac{1}{n}}$, where Q is the constant phase element capacitance, R is the resistance, and n is the non-ideality factor obtained from the fitting procedure. The complex impedance spectra show two dominant semi-circles, one at high and one at low frequency, which when fitted to an equivalent circuit model, yield resistance, and capacitance values, after correcting for the 8% porosity (following the framework presented in Section S5, Supporting Information). Resistance values of 1.51×10^5 and 3.35×10^7 Ω and capacitance values of 2.44×10^{-11} and 4.67×10^{-9} F were extracted at high and low frequencies, respectively, at 141.7 °C. Figure 3c shows the Arrhenius plots of the two resistance contributions, corrected for porosity, allowing one to extract the activation energies for the high (0.7 eV) and low-frequency contributions (1.07 eV), respectively. The activation energy for the high-frequency resistance of 0.7 eV and the magnitude of capacitance of 2.44×10^{-11} F match well with previous reports of the extrinsic bulk ionic conductivity (0.71 eV) and capacitance (1.9×10^{-11} F) in 0.2 at% Gd doped CeO_2[37] with the former relating to the migration enthalpy of oxygen vacancies for a fixed oxygen vacancy concentration, introduced by the Gd dopant according to the following charge balance relation $[Gd'_{Ce}] = 2[V_{\ddot{O}}]$. Here, $[Gd'_{Ce}]$ represents the concentration of Gd^{3+} ions substituted on Ce^{4+} sites, creating net singly negatively charged impurity defects and $[V_{\ddot{O}}]$ represents the concentration of doubly positively charged oxygen vacancies that form for charge compensation. The derived high-frequency capacitance can be confirmed to be associated with the bulk grain properties of this ceria-based material by calculating the dielectric constant from the measured capacitance according to $C = \varepsilon_0 \varepsilon_{bulk}(\frac{A}{nd_g})$, where A is the cross-sectional area, d_g *is* the grain size, and n is the number of grains along the conduction path. Assuming average cubic grains of the same size, and homogenous grain boundaries (400 nm

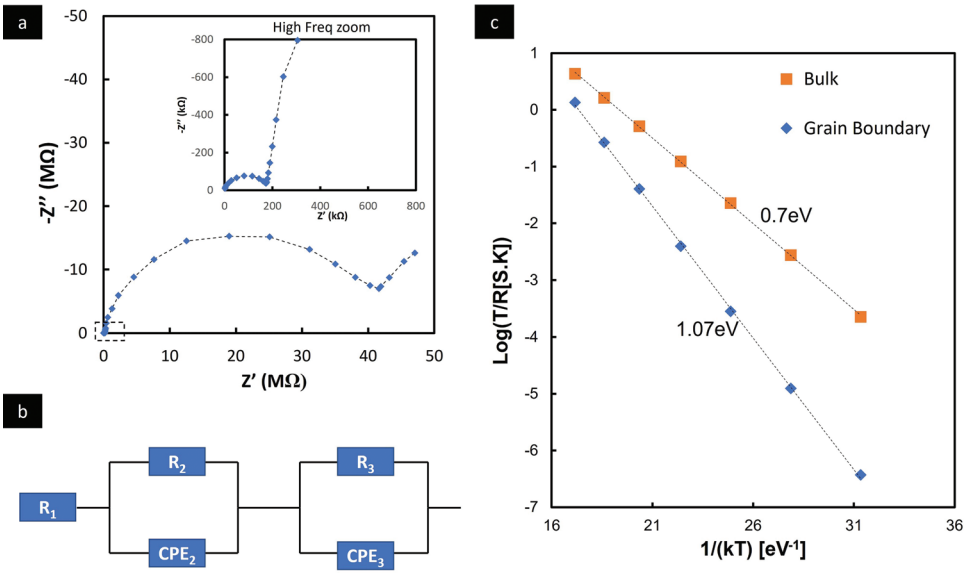

Figure 3. a) Example Nyquist plot of the complex impedance response obtained at 141.7 °C under open-circuit conditions for a 3GDC pellet measured in the dark, with the inset explicitly showing the high-frequency arc. b) Equivalent circuit used to model the circuit elements composed of a resistor in series with 2 R/CPE parallel circuits in series. c) Semi-log plot of the Arrhenius dependence of the conductance G as (1/R) × T versus $1/k_BT$ derived from the high (bulk) and low frequency (grain boundary) arcs.

on average over 1600 grains), we obtain a value of $\varepsilon_{bulk} = 37$, in reasonable agreement with values reported for bulk CeO_2[38] and Gd-doped CeO_2.[38,39] The low-frequency capacitance, on the other hand, matches well with previous reports of grain boundary contributions in Gd-doped CeO_2 (5×10^{-9} vs 4.67×10^{-9} F).[38] In terms of the activation energy, while it is known that the grain boundary activation energy is sensitive to the doping concentration, in the low dopant concentration range, its value matches the expectation for 3GDC observed in previous reports (>1 eV).[40,41]

The total effective grain boundary space charge width δ_{GB}can be estimated from the following equationiom.

$$\delta_{\mathrm{GB}} = \frac{\varepsilon_{\mathrm{GB}}}{\varepsilon_{\mathrm{bulk}}}\left(\frac{C_{\mathrm{bulk}}}{C_{\mathrm{GB}}}\right) d_{\mathrm{g}} \approx \left(\frac{C_{\mathrm{bulk}}}{C_{\mathrm{GB}}}\right) d_{\mathrm{g}} \tag{1}$$

where ε_{bulk} and $\varepsilon_{GB}$are the bulk and grain boundary dielectric constant, d_g is the grain diameter, and C_{bulk} and C_{GB} are the bulk and grain boundary capacitances obtained from the impedance fits. If one assumes that the dielectric constant of the space charge layer ε_{GB} is equal to the bulk dielectric constant (i.e., ε_{bulk}), this then leads to $\delta_{GB} = 2.38$ for 400 nm averaged grain size. This approximation is not unreasonable since the dielectric constant of CeO_2 is insensitive to dopant concentration[37] and the validity of the approximation for ε_{GB} has been experimentally demonstrated for acceptor-doped $SrTiO_3$ in which ε_{GB} was determined to be 0.95 ε_{bulk}.[42] The measured space charge width value also aligns with other reports in the literature for the Gd-doped CeO_2 bulk systems.[27]

In terms of extracting a space charge potential, to first order, assuming a Mott–Schottky scenario where the dopant profile is flat and frozen in during processing, then for large space charge potentials ($\frac{ze\Delta\phi(0)}{k_BT} > 3$), one can use an approximate expression for the grain boundary resistance R_{gb}associated with a space charge potential given by[20,40] (same as Equation S4, Supporting Information):

$$\frac{R_{\mathrm{gb,tot}}}{R_{\mathrm{bulk,tot}}} \approx \frac{\delta_{\mathrm{GB}}}{d_{\mathrm{g}}} \cdot \frac{e^{\frac{ze\Delta\phi(0)}{k_BT}}}{\sqrt{\frac{2ze\Delta\phi(0)}{k_BT}}} \tag{2}$$

where z is the relative charge of the defect (2+ for doubly ionized oxygen vacancies), $\Delta\phi(0)$ is the space charge potential at the grain boundary core, and $R_{gb,tot}$ &$R_{bulk,tot}$are the total GB & bulk resistance contributions respectively. Fitting our results to this expression, we obtain an average space charge potential equal to 0.20 eV, that falls within expected values observed previously in the literature for this material system (> 0.2 eV).[28] The mathematical treatment leading to Equation (2) is similar to the description of the double Schottky barrier model and shows how the grain boundary resistance relates to the bulk resistance with an additional activation energy term for the space charge potential (i.e., $E_{\mathrm{GB}} \sim E_{\mathrm{Bulk}} + \Delta\phi(0)$ where E_{GB} and E_{Bulk} are the activation energies associated with $R_{\mathrm{gb,tot}}$ & $R_{\mathrm{bulk,tot}}$ respectively). While Equation (2) is only an approximation, not valid for small space charge potentials,[40] the general expectation is that when the space charge potential approaches zero, the grain boundary resistance becomes equivalent to the bulk resistance (see Section S2, Supporting Information for additional details). Using the linear fitting of the grain boundary resistance, we can extrapolate the total sample resistance to room temperature, yielding a resistance of 4×10^{12} Ω.

Having established the conductivity of our sample in the dark as the reference, we loaded our sample within its custom-built heater, into our gamma-ray radiation source (see experimental section F for details of setup and Section S6, Supporting Information for details of temperature calibration protocol) to

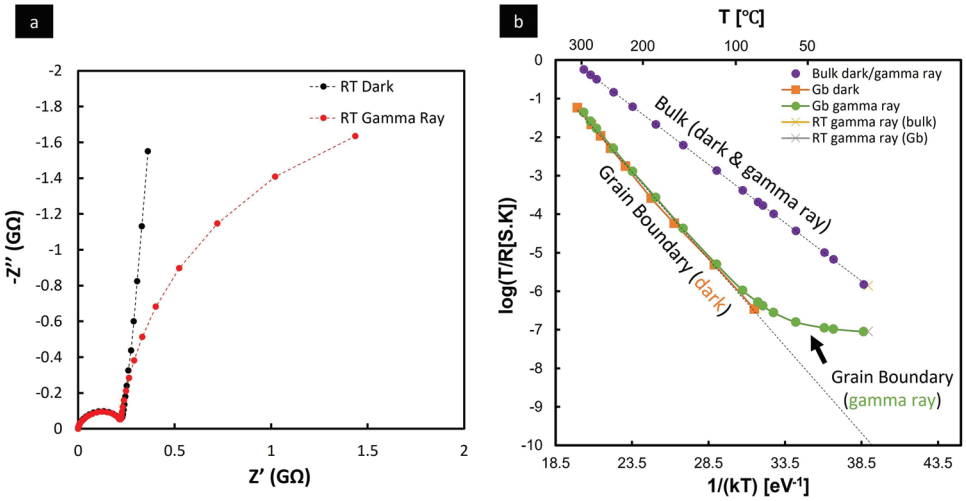

Figure 4. a) Nyquist plots of complex impedance response obtained for the 3GDC pellet measured at near room temperature (≈23.8 °C) in the dark and under γ-rays exposure b) Plot of the Arrhenius dependence of the logarithm of the conductance (1/R) × T versus $1/k_BT$ corresponding to the high frequency and low-frequency arcs (related to grain and grain boundary contributions, respectively) obtained in the dark and under irradiation.

measure the sample's impedance under γ-rays exposure. We plot in **Figure** 4a the near room temperature (≈23.8 °C) impedance spectra obtained for our 3GDC specimen measured both unirradiated (in the "dark") and under γ-ray exposure (dose rate of 35 Gy·min^{-1}), following equilibration for 1 min under irradiation conditions. The impedance under irradiation conditions was measured twice to confirm stability. The observed impedance spectra were fully reversible upon removal from the radiation source, indicating no evidence of degradation under irradiation, with the resistance of the system returning to its dark value within less than seconds of having removed it from the irradiation chamber, allowing the potential γ-ray detector reasonably good time sensitivity.

By examining Figure 4, and the additional close-up in Section S7, Supporting Information, one can make several observations, including 1) the bulk resistance contribution is nearly unchanged under irradiation $\Delta R/R < 1\%$ while 2) the grain boundary resistance at 26.1°C is 3.36×10^9 Ω, a decrease by a factor of ≈680 compared to the dark value. Both contributions' capacitance remained nearly unchanged (Dark: Frequencies $C_{HF} = 2.44 \times 10^{-11}$ F and $C_{LF} = 4.61 \times 10^{-9}$ F, Under γ-ray exposure: $C_{HF} = 3.33 \times 10^{-11}$ F and $C_{LF} = 3.76 \times 10^{-9}$ F). The fact that there was only a negligibly small change in bulk resistance confirms that the specimen remains a predominantly ionic conductor (i.e., low electronic transference number $t_{electronic} << 1$) even under irradiation, with the small observed change, we suspect, tied to radiation-induced heating. The measured change based on the known activation energy would require a temperature change of only ≈0.1 *K*. This finding is similar to the results that we reported for UV irradiation-induced changes in thin film temperatures where we estimated a ≈0.2 *K* increase in sample temperature under an illumination intensity of 630 mW cm^{-2}.[20]

Our measurements show that only the grain boundary resistance is modified under irradiation. Using these observations, we could apply our calibrated temperature curves (see Section S6, Supporting Information for details) to plot the resistance values as a function of temperature under γ-ray exposure. In Figure 4b, we plot the resistances in the dark and under irradiation as a function of temperature. We observe that at higher temperatures (>100 °C), the grain boundary resistance in the dark and under irradiation coincide very well, resulting in an activation energy of 1.07 eV. On the other hand, below ≈100 °C the grain boundary resistance dependence on temperature begins to significantly decrease, leading ultimately to a very shallow effective activation energy of ≈0.08 eV. By extrapolation of the two curves to room temperature, one finds the resistance to be approximately three orders of magnitude lower under irradiation than when unirradiated. By the end of the measurement series, for the lowest temperature (≈26.1 °C), the sample had been continuously irradiated for ≈3 h.

Our conductance data at 26.1 °C under irradiation conditions matches the trend with the data that was obtained at near room temperature (≈23.8 °C) prior to the measurement series, confirming that no degradation could be observed, even following the temperature cycle under irradiation. To further support the reproducibility and reversibility of our observations, we provide additional impedance measurements made prior to, during, and following cycling inside the gamma irradiator, alongside three cycles of single-frequency transient measurements in Figures S14a and S15, Supporting Information that this is consistent with our previous measurement in Figure 4, which confirms the overall stability and reversibility.

3. Discussion

This study demonstrates markedly enhanced ionic conductance in a 3GDC bulk polycrystalline solid electrolyte under penetrating gamma radiation, herewith called the radio-ionic effect. A large decrease in ionic resistance, by a factor of 680 at 26.1 °C for a 35 Gy·min^{-1} irradiation dose rate, indicates strong sensitivity to γ-ray exposure. This originates from the high dark ionic resistance, dominated by the grain boundary resistance, exhibiting a large thermal activation energy (1.07 eV) and the exclusive modification of that grain boundary resistance by gamma-ray

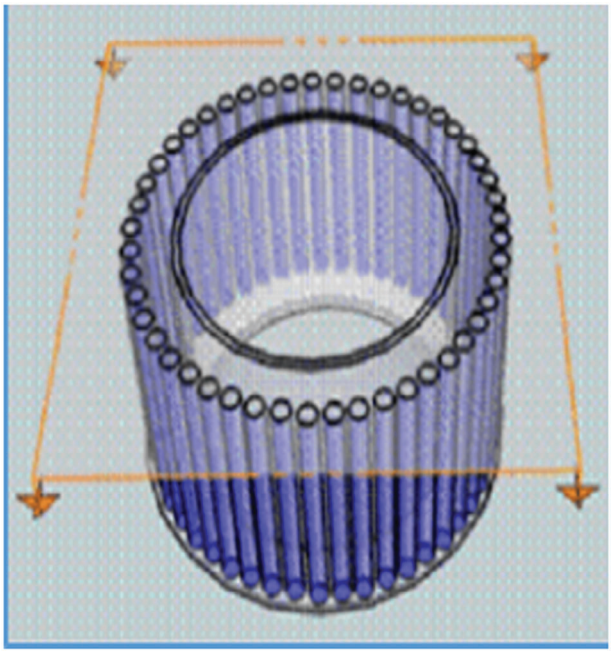

Figure 5. ^{60}Co source array.

irradiation. The fact that the bulk conductivity is barely modified confirms, as observed in the impedance spectra, that 3GDC remains predominantly an ionic conductor throughout the measured temperature range and that more substantial dark versus irradiation conductance ratios can be expected at even lower temperatures. For example, extrapolating the dark grain boundary conductivity according to Equation (2) and the observed grain boundary resistance under irradiation with weak thermal activation energy (0.08 eV) to 21 °C is expected to produce resistance ratios on the order of 1300. Moreover, the unique weak temperature dependence of the grain boundary conductance under irradiation conditions enables robustness to temperature variations. Furthermore, the lack of radiation response in the bulk, and its natural thermally activated behavior, allows us to use higher frequency measurements to monitor the impact of environmental temperature variations on the dark resistance. This allows for improved temperature insensitivity and the design of simple, miniaturized radiation detection devices that can be operated in a variety of environments, without the need for water cooling.

Technologically speaking, while we could earlier demonstrate related opto-ionic response under UV illumination, those results were restricted to thin films, given the strong optical absorption coefficient of 3GDC near its band gap edge. The present radio-ionic effect observations come with inherent advantages: 1) Bulk specimen fabrication is typically simpler and less costly than that of thin films and 2) due to the larger thickness of the specimens (800 microns vs 200 nm), much higher stopping powers can be achieved as needed for the more highly energetic ionizing γ-rays. In contrast to traditional single crystalline semiconductor materials that can only be grown defect-free in limited dimensions and at elevated costs, thick polycrystalline ceramics can be prepared over large areas at low cost, paving the way for creating large-area, cost-effective detector panels. Furthermore, in traditional semiconductor detectors, the electrode geometries, and their separation, need to match charge transport lengths to achieve large responses and fast rates. This relies on the need for photogenerated charge carriers to reach the external circuit before recombining to generate a signal. In our system, instead, the photogenerated electronic carriers need only be trapped at the grain boundaries for ionic conduction modulation to occur. The drift/diffusion lengths are now reduced to the order of grain size dimensions (100′s of nm), rather than electrode spacings of 100′s of microns to multiple mm. In this way, grain boundaries act as virtual electrodes, reducing the effective drift path length required to obtain a signal. This enables the use of materials that typically have very short carrier recombination lifetimes, as well as providing additional flexibility in engineering electrode geometries for such devices. Also, considering the theory associated with light-induced modulation of barrier heights[26] much greater sensitivity can be expected by increasing the dark GB barrier heights, leading to greatly enhanced dark resistivities, leading to lowered background noise. These attributes offer unique opportunities to optimize devices with enhanced sensitivity and operational range and are the subject of ongoing research.

3.1. Reduced Activation Energy at Lower Temperatures

The origin of the shallow activation energy of the grain boundary under γ-rays exposure is surprising as it is far below the activation energy of oxygen vacancy migration within the bulk (≈0.7 eV). Previously in our UV studies on thin films, an activation energy decrease of the effective grain boundary resistance was observed under illumination, with its value coinciding with that of the bulk migration energy of oxygen ions.[20] In the earlier study, while the conductivity under UV irradiation exhibited a bulk-like migration energy, the absolute value of the conductance remained far smaller than that of the epitaxial sample with no grain boundaries. This was explained by noting that not all the space charge barriers responsible for the ion-blocking GBs in 3GDC specimens fully collapsed upon UV illumination. Given the expected distribution of space charge potentials in such polycrystalline samples[41] that originates from the varying tilt angles, grain misorientations,[28] and impurity/dopant segregation,[41] correspondingly higher photogeneration rates are needed to collapse the higher barriers as described by Seager et al. This served as the basis of our development of a constriction model that we describe in detail in ref. [20] and summarize in Section S9, Supporting Information. It specifies that the space charge potential, in only a fraction of the parallel current pathways, is fully collapsed by irradiation for a given radiation intensity. Under UV illumination at 250 °C, for example, we previously calculated that the fully activated cross-sectional area, that is, with space charge potentials brought down to zero, reached values of only ≈3%. Following a similar analysis, the sample resistance at lower temperatures can described according to (Equation (3), same as Equation S9, Supporting Information).

$$\frac{R_{\mathrm{gb,tot}}^{(//)}}{R_{\mathrm{bulk,tot}}} = f_{\mathrm{path}} \tag{3}$$

Figure 6. Gammacell 220.

where $R^{(//)}_{gb,tot}$ is the constricted resistance and f_{path} is a lumped geometrical factor accounting for the decreased conductive area (as compared to the sample's full conductive area) and the tortuosity and the elongation of the pathway. From this relation, we estimate the activated cross-sectional area to be 10% of the total at the lowest measurement temperature (26.1 °C) in our new results.

This still leaves the question of why the measured apparent activation is much lower than the bulk oxygen vacancy migration energy (i.e., 0.7 eV), to be expected for a fully collapsed space charge potential at a grain boundary. Based on our constriction model, we rationalize this observation by considering the fact that the cross-sectional area of the unconstrained conduction pathway (i.e., f_{path}) does not have to remain constant with temperature under constant illumination conditions and could be temperature-dependent. If the parameter f_{path} decreases with increasing temperature, then the activation energy in the low-temperature regime would end up being effectively smaller, reflecting the balance between the increasing bulk ionic migration kinetics versus the decreasing area of the unconstrained conduction path with increasing temperature.

An important question is then: What could be the cause of the temperature dependence of f_{path} and why would it show a negative temperature dependence? To answer this question, we turn to the physics of the electronic charge carrier trapping kinetics at the grain boundaries. We begin by considering the equilibrium recombination velocity at the grain boundary interface, as discussed in Section S11, Supporting Information. The ability of space charge fields to split and collect charges, as well as the core grain boundary traps' capacity to retain trapped charges, are both factors that can be expected to demonstrate negative temperature dependences. Consider that the space charge field weakens with increasing temperature, while the minority carrier capture cross section can be expected to show a negative thermally activated behavior. These combined effects are expected to lead to a significantly negative exponential temperature dependence for the grain boundary recombination kinetics and thereby the f_{path} parameter with temperature. Future studies are needed to investigate the temperature dependence of photo-generated minority charge carrier lifetimes, interface trap energy levels, and grain boundary recombination velocity, to confirm this hypothesis.

3.2. Cause for Reduced Response versus Thin Film

While similar response characteristics were obtained with bulk ceramics under γ-ray exposure compared to thin films under UV illumination,[20] the bulk specimens only exhibited resistance changes below 100°C. In contrast, our previous work on thin films exhibited changes up to 250 °C. Extrapolating our previous thin film results shows that the bulk sample under γ-ray exposure exhibits a smaller response magnitude. While an a priori difference in electronic charge carrier photogeneration rate might exist between the two different sources, even at equal rates, a lower response in the bulk specimen would not be surprising given that our bulk specimens were fabricated via a high-temperature sintering process (1300 °C), with much larger grain sizes (≈400 nm) as compared to those in the thin film samples (50–100 nm). Considering that one should consider the grain boundaries as virtual electrodes, where the opto-ionic effect relies on photogenerated charge carriers being able to reach the grain boundary interfaces at equal photogenerated carrier concentration, a smaller fraction of photogenerated charge carriers would be expected to reach the grain boundaries for considerably larger grain sizes. Thus, a smaller opto-ionic effect in the bulk ceramics should be expected. Future studies examining the impact of grain size on response are planned.

3.3. Material Stability under Applied Bias and Irradiation Conditions

From quantitative analyses of the X-ray diffraction spectra in our study by application of the Rietveld analysis for 3GDC samples B and C irradiated at 500 and 1000 kGy, we find that 3GDC exhibits remarkable radiolytic stability as the crystal structure remained intact (Figure 1 and Section S4, Supporting Information). It can be seen (Table 1 and Table S2, Supporting Information) that there is no detectable change in lattice parameter and volume with increasing γ-ray dose, confirming that the atomic positions remain unaltered. Raman spectroscopy measurements further allowed us to evaluate how the oxygen sublattice's occupancy and the cerium ion's oxidation state might have been impacted by irradiation conditions. As seen in Figure 2, no changes in the main F_{2g} peak and the defect bands, position, or broadness could be observed for any of the samples, strongly supporting the notion that the samples did not undergo any perceivably measurable change in $[Ce^{3+}]$ or $[V_o^{2+}]$ with γ-ray exposure.

Additionally, we also want to address the impact of high electric fields, used traditionally in semiconductor-based detectors for achieving higher electronic charge carrier collection efficiencies, and how this differs from our proposed detection scheme. It is known in ionic systems, for example as reported for halide-based semiconductor detector materials,[43–47] that high fields can

Figure 7. In situ set-up.

lead to polarization of the mobile ionic carriers. On a short time scale, this leads to time-dependent evolution of the detection response, whereas in the long-term, it can lead to electrochemical phase decomposition at the electrodes due to a large pile up of ionic carriers at the blocking electrode interfaces, both effects being undesirable for stable and durable detector operation. However, since our measurements focus solely on the overall sample linear resistance at small volt bias, which relates to ionic conductivity, and not photogenerated charge carriers, there is no need to employ high DC voltages. Instead, we apply a very low magnitude (±200 mV) sinusoidal AC voltage, resulting in very low peak electric field strengths (< 2 V cm^{-1}). This not only minimizes potential point defect generation but also leads to minimal ionic polarization, in stark contrast to traditional semiconductor-based detection that requires high field strengths for efficient charge collection.

Moreover, when comparing our material system to the halide counterparts, that is, $CsPbBr_3$, TlBr, $FAPbBr_3$, and $MAPbI_3$, we note that the latter generally have a rather limited ability to sustain local compositional changes, that can lead to irreversible phase decomposition at the electrodes under applied bias.[48] This is accentuated by the fact that these materials are often incompatible with open-air electrodes, making phase decompositions difficult to reverse and therefore requiring advanced packaging solutions. In contrast, oxide-based material systems are inherently compatible with an open-air environment and can accommodate significant deviations in local stoichiometry without altering the phase or crystal structure. The defect chemistry of oxide materials is commonly studied by examining their conductivity dependence on gas phase oxygen activity at elevated temperatures, and such changes are typically reversible.[49] Therefore, it is theoretically possible to heal stoichiometric changes resulting from extended periods of irradiation and applied bias by annealing the material at elevated temperatures in air.

Collectively, these observations underscore the great potential of ion-conducting polycrystalline ceramic materials applied in radiation detection devices. Moreover, their unique thermal and chemical stability presents unique opportunities for precise γ-ray detection under extreme conditions in various industrial fields, such as nuclear energy solutions, aerospace, oil and gas, and medicine.

4. Conclusion and Outlook

Our findings extend our recently discovered grain boundary optoionic effect observed in solid electrolyte thin films to bulk solid electrolyte ceramics under deeply penetrating gamma radiation. This proof-of-concept paves the way to new all-solid-state radiation detecting devices that rely on the changes in ionic conductance in polycrystalline ceramic solid electrolytes, herewith named the radio-ionic effect. Considering that the majority of defects in these materials are already ionic in nature, by leveraging the interaction between photogenerated charge carriers and the ionic migration barriers present at grain boundaries, we develop a sensing response that relies on and benefits from structural defects. Owing to the blocking nature of the grain boundaries, the polycrystalline sample's dark resistance can be orders of magnitude higher than the bulk values, reaching values as high as $> 10^{12}$ Ω near room temperature, favorable for achieving high sensitivities of $\Delta R/R \geq 10^3$. This response can be further enhanced by modulating the dark grain boundary resistance by moving towards nanocrystalline systems or engineering the grain boundary properties to enhance the space charge potential heights. Furthermore, photogenerated electronic charges that remain as minority defect carriers in the material need only drift/diffuse very short distances (typically sub-micron) to reach the grain boundaries where they interact with the migration barriers that impede ionic motion. In essence, the grain boundaries that trap the electronic charge carriers act as virtual electrodes. This enables a large fraction of photogenerated charge carriers to participate in the sensing response with fast response rates, even for moderate electronic mobilities. In that sense, the criteria for developing a strong sensing response differs from traditional semiconductor materials engineered to prevent their photogenerated charges from trapping. We, on the other hand, favor the trapping process explicitly at the grain boundaries. Our findings open a broad new category of materials suitable for radiation detection composed of large band gap (> 3 eV), high Z (> 60), and easy-to-handle oxide-based ceramics that can be manufactured at low cost as thick and large area devices. Further advantages include utilizing low-cost polycrystalline oxide materials while exhibiting high stability in ambient and elevated temperatures. The chemical and generally high-temperature stability of oxide materials opens new opportunities for designing radiation detectors for high-temperature and/or corrosive/high-pressure environments, desirable features in next-generation nuclear technology solutions such as geothermal directional drilling, small modular nuclear reactors, nuclear

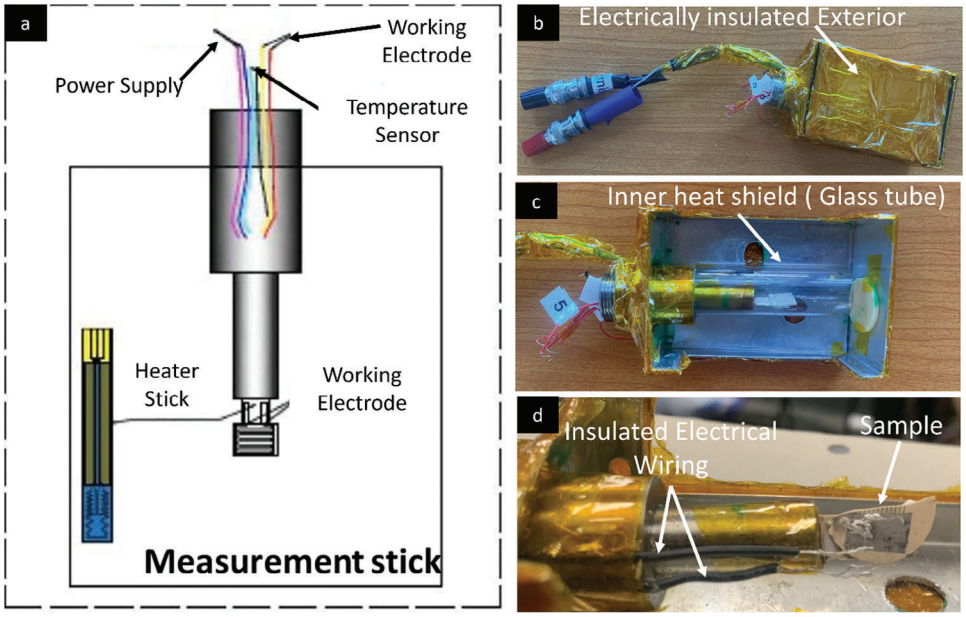

Figure 8. a) Schematic of in situ heater/measurement device with b) photo of its electrically insulated exterior, c) inner heat shield, and d) insulated electrical wires connecting the sample to the electrical testing equipment. The structure of the heater stick, consisting of screen-printed gold contacts, back side Pt-heater lines, and a front side Au–Pt thermocouple on an alumina substrate, is a simplified setup of the direct thermoelectric gas sensor as shown in ref. [53].

security, and waste management. Moreover, grain boundary resistivities, as they relate to space charge effects, have also been reported for many well-known lithium, sodium, and proton solid-state ion conductors. This opens many new materials opportunities for determining optimum detection response and for reducing materials synthesis costs, as well as designing radiation detection schemes selective to alternative ionizing radiation (e.g., alpha, neutrons, X-ray).

5. Experimental Section

Sample Preparation: The $Gd_{0.03}Ce_{0.97}O_2$ (3GDC) powder was synthesized by a solution combustion route, starting from $Ce(NO_3)_3{\cdot}6H_2O$ (99.99%, Alfa Aesar), $Gd(NO_3)_3{:}6H_2O$ (Strem Chemicals) (99.99%) precursors, and citric acid. The solution was heated on a hot plate, and following gel combustion, the reaction resulted in the formation of a whitish powder. The resulting GDC powders were calcined at 900 °C for 1 h to obtain the GDC powder crystallized in the fluorite structure. The powder was then pressed into a 30 mm diameter disk with a uniaxial press (1 Tcm^{-2}) and sintered at 1300 °C for 8 h, followed by cooling at 1 °C min^{-1} to limit crack formation, resulting in a pellet with 92% density. 100 nm thick platinum electrodes were subsequently DC sputtered on either side of the pellet using Kapton tape to serve as a shadow mask covering a rectangular area of 5 × 9 mm. The electrode was subsequently attached to Pt wires in both the furnace setup and custom-built microheater device using a commercial Ag paste purchased from Fuel Cell Materials (#321201) and dried using a hand-held heat gun for 10 min and then subsequently dried in a furnace to 450 °C while holding for 1 h.

Material Characterization (XRD/SEM/Raman): X-ray diffraction patterns were obtained with a Rigaku SmartLab with Cu Kα rotating anode source in a coupled scan. To determine the lattice parameters of irradiated GDC samples, we performed Rietveld refinement using High Score Plus software. Refinement quality can be determined using different statistical parameters, such as goodness of fit. We continued the refinement process until the convergence became close to 1 or reached the lowest number. The structural properties of GDC before and after γ-rays exposure are tabulated in Table 1 and Table S1, Supporting Information.

SEM Images of the cross-sections of the device sample after freshly fracturing the surface were acquired on a Zeiss Merlin high-resolution scanning electron microscope. A Matlab script developed by A. Rabbani et al[50,51] was used to analyze the image's grain size.

Raman spectroscopy was employed to study the vibrational modes of oxygen-cation bonds, sensitive to both the oxidation state of the cation and the site occupancy of the anion, useful in corroborating phase purity and for investigating defect formation under high irradiation doses. Techniques such as XPS, to directly measure the oxidation state of the cations, were not employed due to the surface sensitivity of the tools, and the knowledge from existing literature reports that indicate that the concentration of mixed-valent elements at the top several nanometers from the surface can be orders of magnitude higher than in the bulk even without irradiation.[52] A Renishaw Invia Reflex Micro Raman was employed with a 50× objective yielding a 10-micron spot size, with a spectral resolution of ±0.5 cm^{-1}, and laser power of 5 mW. An excitation wavelength of 473 nm (2.63 eV) was selected. The data were analyzed by fitting the peak curves and subtracting the baseline to remove the background. The data was then normalized by the highest peak intensity.

MIT Cobalt-60 Gamma Irradiation Facility: The MIT Core User Facility γ-ray irradiator was used to irradiate the test sample in situ . The irradiator was a Gammacell 220 Excel self-shielded high dose rate irradiator manufactured by MDS Nordion on 10/13/2003 containing an initial quantity of cobalt-60 (^{60}Co) of 375.2 terabecquerel (TBq) and a current activity of 97.3 TBq. The current irradiation dose rate was ≈35 Grey min^{-1}. The ^{60}Co sources were arranged in a caged array allowing for a uniform dose of the materials being irradiated (**Figure 5**). The ^{60}Co sources were contained within a lead biological shield which allowed for the safe use of the irradiator by trained radiation workers. The sample to be irradiated was transported by an internal elevator into the source array. The irradiator was equipped with a top shield plug that can be adjusted to allow the insertion of cabling to perform the in situ investigations. The test sample was loaded into the sample irradiation chamber (**Figure 6**). The sample chamber was

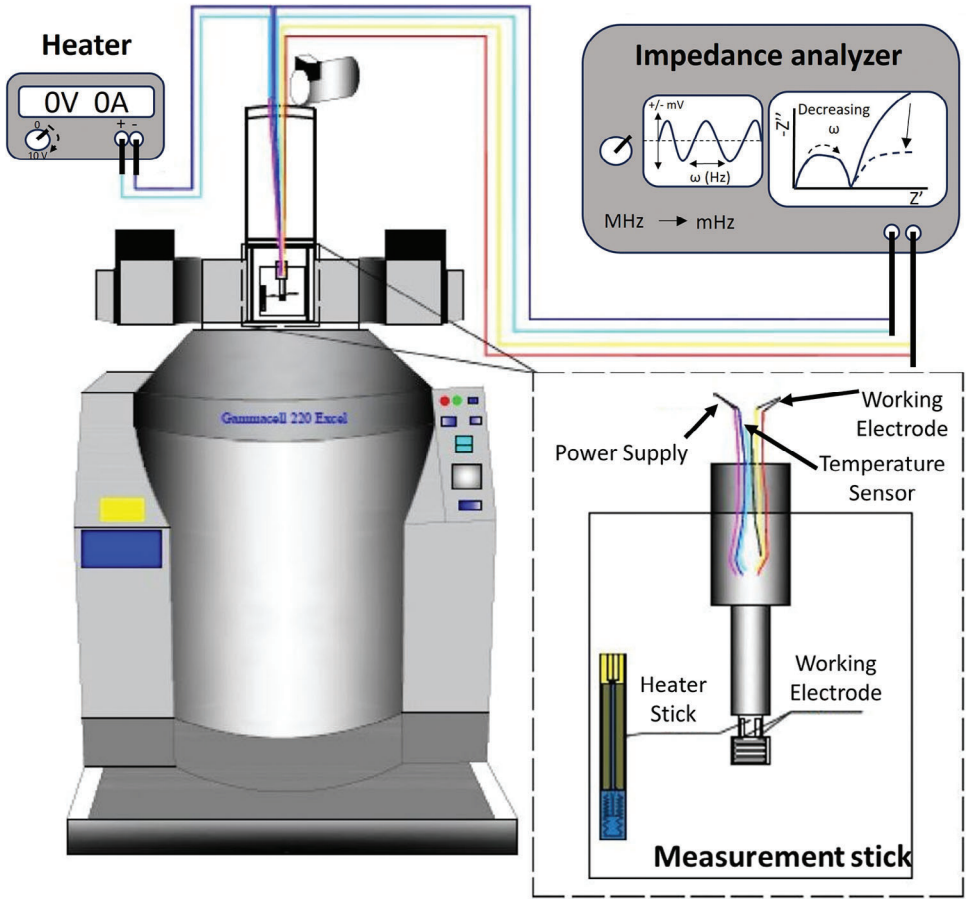

Figure 9. The in situ heater/measurement device, composed of the heater stick, is connected to a power supply rated for (10 V/0.5 A) and an impedance analyzer. The heater stick device would sit inside the reactor's main chamber and be connected through the top. To begin the experiment, the main chamber was automatically lowered into the body of the irradiator where it was exposed to the ^{60}Co source array.

a thin-walled, closed, non-porous metal cylinder with a full-width door. The inside dimensions of the chamber were 6.10 inches (15.49 cm) in diameter and 8.06 inches (20.47 cm) high. The test article was connected to our analysis equipment via the top shield plug raceway and lowered by elevator into the ^{60}Co source array (**Figure 7**). The system could be operated in both an automatic and manual modes. In manual mode, the user controlled the irradiation and retrieval of the sample chamber. The in situ experiments required operation in manual mode to allow the cycling of the test article in and out of the radiation field.

Radiation Safety: All personnel using the MIT γ-ray irradiation facility were required to register their projects for review and approval by the MIT Radiation Protection Committee. Individual users must complete an irradiator-specific radiation safety course accompanied by site-specific training, which included hands-on instruction on the use of the irradiator as well as security and emergency response training. Annual retraining was required for all users. All users were monitored for potential radiation exposure and required to wear radiation dosimetry when using the irradiation facility. Only trained radiation workers qualified as trustworthy and reliable could gain unescorted access to the facilities.

Security: The irradiator facility had an extensive access control and security system. MIT Police, Facilities Operations Center monitored security and radiation alarms continuously (24 h per day). The MIT Radiation Protection Program (RPP) was on-call to assist in response to alarm conditions.

Measurement Setup—Custom-Built Heater Stick: As displayed in **Figure 8**, the in situ heater/measurement device was composed of a heater stick made of an alumina plate with screen-printed electrical tracks (Pt) on the bottom for heating and Au/Pt thermocouple tracks on top for accurate temperature sensing. This is a simplified setup of the direct thermoelectric gas sensor as shown in ref. [54] This heater stick was inserted inside a cylindrical stainless-steel pipe which itself was inserted inside a Swagelok stainless steel Ultra-Torr Vacuum Fitting (RA-TORR SS), such that all the temperature control and sensor wires would exit the back end of the pipe (away from the sample). This assembly was inserted into a stainless-steel box with a custom hole drilled on one end for the back end of the Swagelok fitting to stand out with its wires. The box could be manually opened for easy sample access. The box was surrounded by Kapton tape on all sides to allow for electrical insulation with its surroundings. A borosilicate glass tube was put around the heater to act as a heat shield and prevent partial thermal leakage. Two insulated electrical leads supporting electrical conductivity measurement (impedance) were then connected to the sample electrodes that had previously been bonded to the Sputtered Pt pads using silver paste. These wires were connected externally to BNC connectors to enable a secured connection to the electrical testing equipment.

The sample pellet was bonded to the custom-built mini-heater device with a ceramic paste (Ceram-Bond) that was first dried with a hand-held heater gun for 150 min and then subsequently dried by heating the heater stick up to 300 °C and held for 1 h. The actual sample temperature in such a custom heater stick was then calibrated according to the protocol described in Section S6, Supporting Information.

Measurement Setup—Electrical Measurements: As shown in **Figure 9**, the custom-built mini-heater device was inserted inside the Gammacell 220 testing chamber and connected both to a impedance ananalyzer and power supply. Measurements were performed by continuously irradiating

the sample at a dose rate of 35 Gy min^{-1} and heating up to the highest temperature, then measuring the impedance on the way back down incrementally and allowing the sample to equilibrate for 5 min at each temperature step. All EIS measurements were performed with an Autolab PGSTAT302N Impedance Analyzer. A 200 mV amplitude was necessary to achieve a sufficient current response in the highly resistive samples. The frequency range was 0.01 Hz to 1 MHz.

Supporting Information

Supporting Information is available from the Wiley Online Library or from the author.

Acknowledgements

T.D. and H.T. acknowledge support by the U.S. Department of Homeland Security, Countering Weapons of Mass Destruction Office, under awarded grant 22CWDARI00046. J.L. acknowledges support by DTRA (Award No. HDTRA1-20-2-0002) Interaction of Ionizing Radiation with Matter (IIRM) University Research Alliance (URA), and the U.S. Department of Homeland Security. This support does not constitute an express or implied endorsement on the part of the Government. T.D. and A.S.H. would like to thank Mitchell S. Galanek and Bob Kirby from the Office of Environment, Health & Safety at the Massachusetts Institute of Technology for their assistance with managing safety during radiation experiments.

Conflict of Interest

The authors declare no conflict of interest.

Author Contributions

T.D., J.L., J.L.M.R., and H.L.T. designed the concept and research. T.D. and A.S.H. designed the experimental research protocols. T.D. performed the research and analyzed the data with A.S.H. support. T.D. and H.L.T. wrote the paper and J.L. and J.L.M.R. provided edits and revisions..

Data Availability Statement

The data that support the findings of this study are available from the corresponding author upon reasonable request.

Keywords

electroceramics, polycrystalline, radiation detection, radiation-ionic, solid electrolytes

Received: September 8, 2023
Revised: January 26, 2024
Published online:

[1] S. Yakunin, D. N. Dirin, Y. Shynkarenko, V. Morad, I. Cherniukh, O. Nazarenko, D. Kreil, T. Nauser, M. V. Kovalenko, *Nat. Photonics* **2016**, *10*, 585.
[2] Y. He, M. Petryk, Z. Liu, D. G. Chica, I. Hadar, C. Leak, W. Ke, I. Spanopoulos, W. Lin, D. Y. Chung, B. W. Wessels, Z. He, M. G. Kanatzidis, *Nat. Photonics* **2021**, *15*, 36.
[3] K. Hitomi, Y. Kikuchi, T. Shoji, K. Ishii, *IEEE Trans. Nucl. Sci.* **2009**, *56*, 1859.
[4] A. Datta, P. Becla, S. Motakef, *Sci. Rep.* **2019**, *9*, 2439.
[5] J. Mizusaki, K. Arai, K. Fueki, *Solid State Ionics* **1983**, *11*, 203.
[6] Z. Xu, R. A. Kerner, S. P. Harvey, K. Zhu, J. J. Berry, B. P. Rand, *ACS Energy Lett.* **2023**, *8*, 513.
[7] K. E. Sickafus, R. W. Grimes, J. A. Valdez, A. Cleave, M. Tang, M. Ishimaru, S. M. Corish, C. R. Stanek, B. P. Uberuaga, *Nat. Mater.* **2007**, *6*, 217.
[8] F. Garciá Ferré, A. Mairov, L. Ceseracciu, Y. Serruys, P. Trocellier, C. Baumier, O. Kaïtasov, R. Brescia, D. Gastaldi, P. Vena, M. G. Beghi, L. Beck, K. Sridharan, F. Di Fonzo, *Sci. Rep.* **2016**, *6*, 33478.
[9] S. J. Zinkle, G. S. Was, *Acta Mater.* **2013**, *61*, 735.
[10] D. Zhu, M. Nikl, W. Chewpraditkul, J. Li, *J. Adv. Ceram.* **2022**, *11*, 1825.
[11] C. Greskovich, S. C. S. Duclos, *Annu. Rev. Mater. Sci* **1997**, *27*, 69.
[12] R. M. Sahani, A. Dixit, *Mater. Sci. Semicond. Process.* **2022**, *151*, 107040.
[13] I. Hany, G. Yang, C. C. Chung, *J. Mater. Sci.* **2020**, *55*, 9461.
[14] P. Knauth, H. L. Tuller, *J. Am. Ceram. Soc.* **2002**, *85*, 1654.
[15] Y. Zhu, J. C. Gonzalez-Rosillo, M. Balaish, Z. D. Hood, K. J. Kim, J. L. M. Rupp, *Nat. Rev. Mater.* **2021**, *6*, 313.
[16] S. J. Skinner, J. A. Kilner, *Mater. Today* **2003**, *6*, 30.
[17] R. Devanathan, *Nucl. Instrum. Methods Phys. Res., Sect. B* **2009**, *267*, 3017.
[18] S. J. Zinkle, E. R. Hodgson, *J. Nucl. Mater.* **1992**, *191–194*, 58.
[19] US NRC. Standard Review Plan for the Review of Safety Analysis Reports for Nuclear Power Plants: LWR Edition. NUREG-0800, **2021**.
[20] T. Defferriere, D. Klotz, J. C. Gonzalez-Rosillo, J. L. M. Rupp, H. L. Tuller, *Nat. Mater.* **2022**, *21*, 438.
[21] D. Pergolesi, E. Fabbri, A. D'Epifanio, E. Di Bartolomeo, A. Tebano, S. Sanna, S. Licoccia, G. Balestrino, E. Traversa, *Nat. Mater.* **2010**, *9*, 846.
[22] G. Gregori, R. Merkle, J. Maier, *Prog. Mater. Sci.* **2017**, *89*, 252.
[23] D. P. Joshi, K. Sharma, *Indian J. Pure Appl. Phys.* **2012**, *50*, 661.
[24] J. P. Salerno, R. W. McClelland, J. G. Mavroides, *MRS Online Proceedings Library* **1982**, *14*, 375.
[25] M. K. Sharma, D. P. Joshi, *Indian J. Pure Appl. Phys.* **2010**, *48*, 575.
[26] C. H. Seager, *J. Appl. Phys.* **1981**, *52*, 3960.
[27] D. P. Joshi, D. P. Bhatt, *IEEE Trans. Electron Devices* **1990**, *37*, 237.
[28] H. J. Avila-Paredes, K. Choi, C. T. Chen, S. Kim, *J. Mater. Chem.* **2009**, *19*, 4837.
[29] S. Kim, S. K. Kim, S. Khodorov, J. Maier, I. Lubomirsky, *Phys. Chem. Chem. Phys.* **2016**, *18*, 3023.
[30] X. Guo, R. Waser, *Prog. Mater. Sci.* **2006**, *51*, 151.
[31] J. Kim, S. J. Pearton, C. Fares, J. Yang, F. Ren, S. Kim, A. Y. Polyakov, *J. Mater. Chem. C* **2018**, *7*, 10.
[32] R. Rasmidi, M. Duinong, F. P. Chee, *Radiat. Phys. Chem.* **2021**, *184*, 109455.
[33] T. Shikama, M. Narui, Y. Endo, T. Sagawa, H. Kayano, *J. Nucl. Mater.* **1992**, *191*, 575.
[34] E. R. Hodgson, *J. Nucl. Mater.* **1992**, *191*, 552.
[35] G. P. Pells, B. C. Sowden, *J. Nucl. Mater.* **1995**, *223*, 174.
[36] J. L. M. Rupp, A. Infortuna, L. J. Gauckler, *Acta Mater.* **2006**, *54*, 1721.
[37] T. C. Yeh, N. H. Perry, T. O. Mason, *J. Am. Ceram. Soc.* **2011**, *94*, 1073.
[38] R. Schmitt, A. Nenning, O. Kraynis, R. Korobko, A. I. Frenkel, I. Lubomirsky, S. M. Haile, J. L. M. Rupp, *Chem. Soc. Rev.* **2020**, *49*, 554.
[39] A. Tschöpe, E. Sommer, R. Birringer, *Solid State Ionics* **2001**, *139*, 255.
[40] M. Vollman, R. Waser, *J. Am. Ceram. Soc.* **1994**, *77*, 235.
[41] X. Tong, D. S. Mebane, R. A. De Souza, *J. Am. Ceram. Soc.* **2020**, *103*, 5.
[42] A. Tschöpe, S. Kilassonia, R. Birringer, *Solid State Ionics* **2004**, *173*, 57.

[43] X. Xu, Y. Liu, J. Wang, D. Isheim, V. P. Dravid, C. Phatak, S. M. Haile, *Nat. Mater.* **2020**, *19*, 887.
[44] C. Chen, Q. Fu, P. Guo, H. Chen, M. Wang, W. Luo, Z. Zheng, *Mater. Res. Express* **2019**, *6*, 115808.
[45] L. Pan, I. R. Pandey, Z. Liu, J. A. Peters, D. Y. Chung, C. Hansson, B. W. Wessels, A. Miceli, M. G. Kanatzidis, *J. Appl. Phys.* **2023**, *133*, 194502.
[46] A. Y. Grishko, M. A. Komkova, E. I. Marchenko, A. V. Chumakova, A. B. Tarasov, E. A. Goodilin, A. A. Eliseev, *Nano Res.* **2023**, *16*, 9435.
[47] V. Kozlov, M. Kemell, M. Vehkamäki, M. Leskelä, *Nucl. Instrum. Methods Phys. Res., Sect. A* **2007**, *576*, 10.
[48] A. Datta, S. Motakef, *IEEE Trans. Nucl. Sci.* **2015**, *62*, 1244.
[49] A. Senocrate, G. Y. Kim, M. Grätzel, J. Maier, *ACS Energy Lett.* **2019**, *4*, 2859.
[50] H. L. Tuller, S. R. Bishop, *Annu. Rev. Mater. Res.* **2011**, *41*, 369.
[51] A. Rabbani, S. Salehi, *J. Nat. Gas Sci. Eng.* **2017**, *42*, 157.
[52] C. P. Ezeakacha, A. Rabbani, S. Salehi, A. Ghalambor, in *SPE Int. Symp. on Formation Damage Control Lafayette*, LA, USA, **2018**.
[53] C. B. Gopal, F. E.l Gabaly, A. H. McDaniel, W. C. Chueh, *Adv. Mater.* **2016**, *28*, 4692.
[54] D. Chen, A. Groß, D. C. Bono, J. Kita, R. Moos, H. L. Tuller, *Solid State Ionics* **2014**, *262*, 914.

ADVANCED MATERIALS

Supporting Information

for *Adv. Mater.*, DOI 10.1002/adma.202309253

Ionic Conduction-Based Polycrystalline Oxide Gamma Ray Detection – Radiation-Ionic Effects

Thomas Defferriere, Ahmed Sami Helal, Ju Li*, Jennifer L. M. Rupp* and Harry L. Tuller**

Ionic-conduction based Polycrystalline Oxide Gamma Ray Detection - Radiation-ionic Effects

Supplementary Information

Table of Contents

I. Bulk Ionic Transport

The detailed physics associated of bulk and grain boundary ionic transport in polycrystalline ionic conductors have been previously described[1–4], but we summarize key features in supplementary sections **I** and **II** for the benefit of the Reader.

Ion transport in solid electrolytes is a thermally activated hopping process and if we neglect microstructural effects, then the bulk ionic conductivity σ_{ion} can be defined to a first approximation as:

$$\sigma_{ion} = c_i . q_i . \mu_i = c_i . q_i . \mu_0 \exp\left(-\frac{\Delta H_{m,i}}{kT}\right) \quad (S1)$$

Where c_i is the concentration of mobile ionic species i, qi their net charge, μ_i their mobility, μ_0 the mobility preexponential term, k the Boltzmann constant, T temperature in degrees Kelvin, $\Delta H_{m,i}$ the migration enthalpy. Doping to introduce lattice defects is a common strategy to enhance c_i but comes with drawbacks due either to limited dopant solubility, or in the case of highly doped systems (~ >5-10 at%), defect-dopant association or longer-range defect ordering that contribute to higher $\Delta H_{m,i}$. In this study we focus on Gd doped CeO_2, an oxygen ion conductors where oxygen ions migrate through the lattice by hopping via mobile oxygen vacancy sites ($V_O^{\cdot\cdot}$), introduced into the systems by addition of the substitutional dopant Gd'_{Ce}, with net negative charge to the lattice, through the following charge balance relation: $[Gd'_{Ce}] = 2[V_O^{\cdot\cdot}]$. The migration enthalpy is known to range from 0.7-0.9eV depending on the doping level of the system.

II. Interfacial Ionic Transport in Polycrystalline Solids

While solid electrolytes and their selected dopant levels are often optimized to achieve the highest ion conductivities, the fact is that the materials used, are polycrystalline. These grain boundaries often act as barriers to the flow of ions between the grains, leading at times, to many orders of magnitude increases in ionic resistivity. Over the years, with many efforts in powder purification, it has been shown that the resistance of the grain boundary remains intrinsic and relates to space charge barriers that develop due to the presence of net charges in the core of the grain boundaries (due, for example, to segregation of charged impurities) result in built-in electric fields in the adjacent grains[1]. These fields induce a redistribution of mobile charged defects in a so-called space charge zone. The physics is no different than space charge effects at grain boundaries in electronic semiconductors (e.g., polycrystalline Si or Ge) with a major difference being the nature of the mobile charge carriers (for semiconductors, electrons and holes while for wide band gap solid electrolytes, ionic defects). For ionic conductors, the majority ionic carriers become depleted in the space charge zone, resulting in orders of magnitude higher local ionic resistances. We consider here a simplified dilute limit picture and apply the Mott-Schottky case to describe the space charge zone[1,3,4]. In this model the dopant profile is assumed flat and frozen-in during processing, and only the oxygen vacancies can redistribute within the proximity of the grain boundary. The spatial profiles of the charged majority oxygen vacancy and minority electronic species are shown in **Figure** S1.

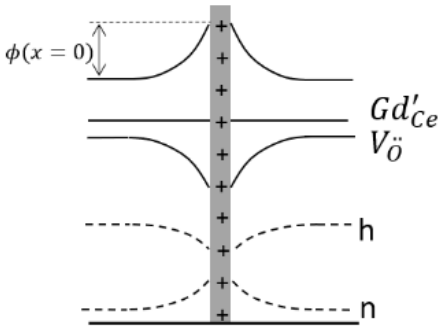

Figure S1 *Schematic of a space charge zone in acceptor doped (Gd) CeO_2 in air a low temperature (<300ºC) A positive core charge results in the depletion of positively charged mobile carriers ($v_o^{\cdot\cdot}$ and h) and the accumulation of negatively charged mobile carriers (n). A Simplified Mott Schottky approximation is considered where the dopant profile is assumed to be flat and frozen-in, and where the dopant is not able to redistribute during the measurement conditions.*

The corresponding Boltzmann distribution expression describing the distribution of carriers is given in Equation S2 with z being the relative charge of the defect, c_{gb} & c_{bulk} the grain boundary and bulk defect concentrations and $\Delta\phi_{gb}(x)$ the spatially dependent grain boundary potential[1]. Note that the majority ionic oxygen vacancy defect concentration and electronic hole defect are depleted, while the minority electron concentration *n* is accumulated within the space charge region.

$$\frac{c_{gb}(x)}{c_{bulk}} = e^{-\frac{ze\Delta\phi(x)}{k_B T}} \tag{S2}$$

The conductivity of the grain boundary across the space charge zone can then be defined as:

$$\sigma_{gb}(x) = \sigma_{bulk} e^{-\frac{ze\Delta\phi(x)}{k_B T}} \tag{S3}$$

which describes how the space charge zone conductivity relates to the bulk conductivity (σ_{bulk}) and the depletion of ionic carriers within the depletion zone following the spatial distribution of the space charge potential in the vicinity of the interface. Eq. S3 shows that as space charge potential tends to zero then the grain boundary conductivity tends toward the bulk conductivity.

The potential distribution is found by solving Poisson's equation, but no exact analytical solution can be obtained[3]. One can, however, derive an approximate expression in the case of sufficiently large space charge potentials (i.e., $\frac{2ze\Delta\phi(0)}{k_B T}$>3). In the Mott-Schottky case the expression for grain boundary resistance and its relation to the space charge potential in the grain boundary core ($\Delta\phi(0)$) can be obtained by integrating Eq. S3, yielding (Eq. S4 - same as Eq. 2 in main manuscript):

$$\frac{R_{gb,tot}}{R_{bulk,tot}} \approx \frac{\delta_{GB}}{d_g} \cdot \frac{e^{\frac{ze\Delta\phi(0)}{k_B T}}}{\frac{2ze\Delta\phi(0)}{k_B T}} \tag{S4}$$

Where d_g is the grain edge length (assuming a simplified brick layer model) and δ_{GB} is the effective grain boundary space charge width, defined as $\delta_{GB} = 2\lambda$, where we typically neglect the grain boundary core contributions and λ being the Mott-Schottky space charge width:

$$\lambda = 2\left(\frac{kT\varepsilon}{2e^2\left[Gd'_{Ce,bulk}\right]}\right)^{0.5}\left(\frac{e\Delta\phi(0)}{kT}\right)^{0.5} \quad \text{(S5)}$$

which relates to the Debye length L_D (first term in Eq. S5 in parenthesis) and the space charge potential. Expression S4 and S5 are approximations for the Mott-Schottky case. It is also possible to derive an approximate solution for another scenario, called the Gouy-Chapman case, that considers the dopant to also be mobile and able to redistribute in the space charge zone throughout the measurement conditions. In that case, the space charge width is smaller and equates to the Debye length (i.e $\lambda = L_D$). The Gouy-Chapman case, however, is only valid in ceria when the dopant is mobile which is typically only true at elevated sintering temperatures (> 1000°C) and is generally not considered for lower temperature conductivity measurements, warranting the use of the Mott-Schottky approximation[5]. It should be noted that the Mott-Schottky approximation can lead to large errors on the extracted grain boundary space charge potential from conductivity data, as non-uniform concentrations of the dopant profile in the grain boundary vicinity arise during high temperature processing conditions and end up subsequently frozen in upon cooling. This leads to a so-called *restricted equilibrium* scenario[5], which is out of equilibrium and lies between the Mott-Schottky and Gouy-Chapman cases. This can only be evaluated via numerical simulations and knowledge of the dopant profile frozen in - impractical for most experimental studies.

It is also worth noting that while most studies of GB resistivity in ionic conductors derive a single effective barrier potential, GBs in a given solid are known to differ, depending on the misorientation angle between adjacent grains, impacting impurity and defect segregation, leading ultimately to a broad range of GB potentials[6] that cannot be easily distinguished from simple electrical measurements. This is exacerbated by the fact that electrical measurement techniques measure the weighted average of all current paths across the numerous grain boundaries, dominated by the paths of least resistance[5]. This implies that the use of an approximate analytical solutions for the fitting of grain boundaries space charge potentials based on electrical measurements are mainly used to consider general trends and for the sake of discussion, as we do in this study.

III. Structural Characterization

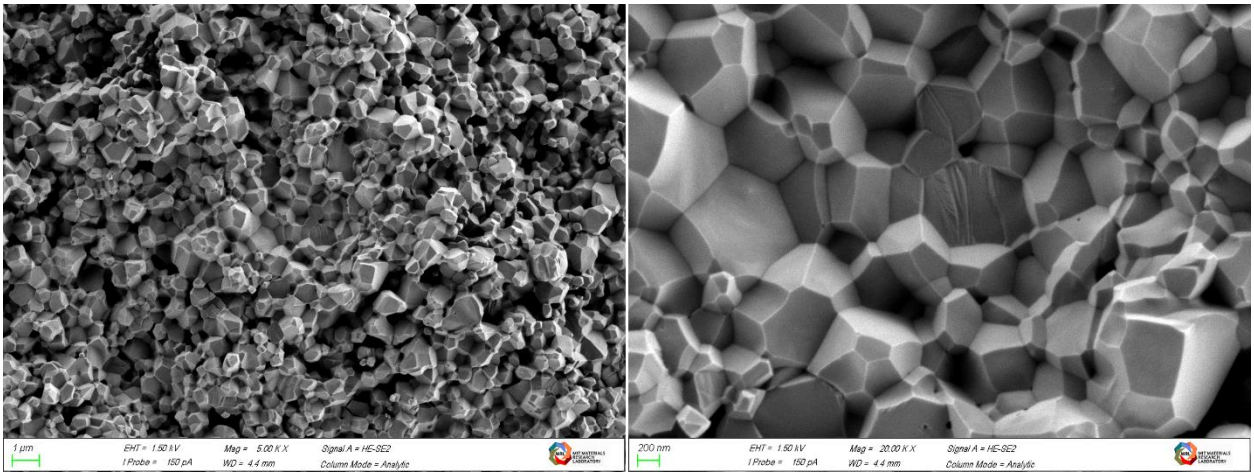

Figure S2- *SEM micrograph of fracture surface of pristine polycrystalline 3GDC pellet.*

Figure S2 shows the SEM micrograph of the fractured surface of the pristine polycrystalline 3GDC pellet. Using a Matlab script developed by A. Rabbani et al [7,8] for analyzing the grain structure from the image, we obtain an average grain size ~ 400 nm.

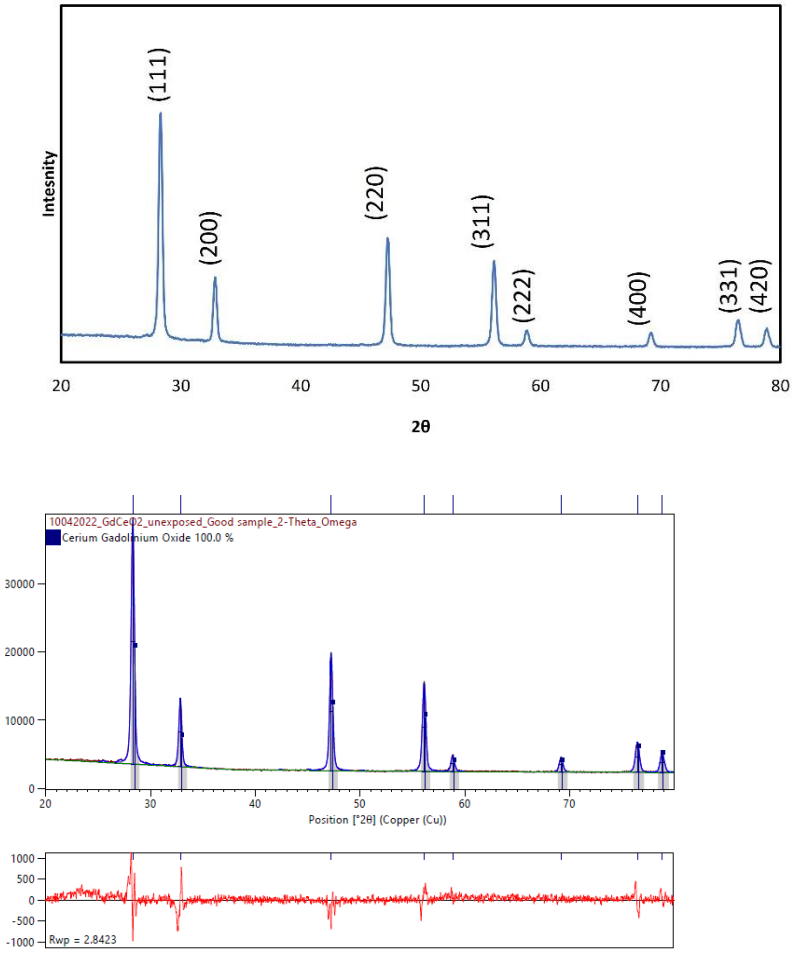

Figure S3- *(Top) XRD results for the 3GDC pellet sintered at 1300 ℃ (Bottom) Rietveld fitting methods results.*

The XRD results of the pristine 3GDC pellet sintered at 1300 C is shown in **Figure** S 3. The sample showed reflection peaks (1 1 1), (2 0 0), (2 2 0), (3 1 1), (2 2 2), (4 0 0), (3 3 1) and (4 2 0) at 2θ of 28.30, 32.85, 47.25, 56.13, 58.86, 69.21, 76.49 and 78.87 respectively. From the Rietveld fitting, one concludes that the XRD pattern agrees with expectations for the face-centered cubic structure of CeO_2.

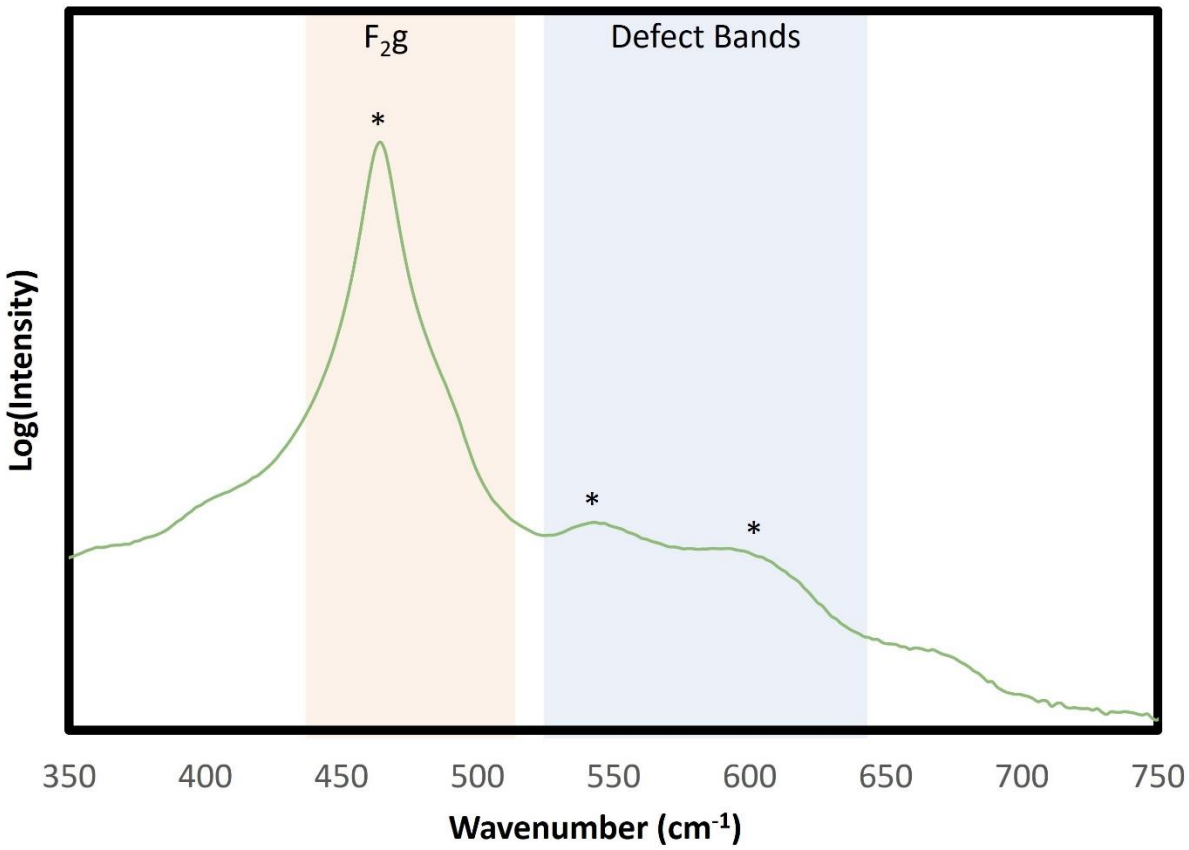

Figure S4 *Raman results for the pristine 3GDC pellet sintered at 1300 ℃ recorded using 473 nm wavelength illumination. Major peaks of interest are situated at 464.24 cm^{-1}and around ~550/600 cm^{-1}and are indicated by an *.*

Figure S4 shows the Raman spectra of the surface of the GDC pellet recorded using 473 nm wavelength illumination. The major peak at 464.24 cm^{-1} is consistent with the symmetric oxygen breathing mode around the Ce^{4+} cation with F_2g symmetry and relates to bond length changes between O-Ce-O.[9] On the other hand, the two peaks around ~550/600 cm^{-1} have generally been associated with the presence of the dopant ions and oxygen vacancies, but their exact origin remains a source of debate[9]. The peak at 550 cm^{-1} has been shown to exist only when oxygen vacancies are present in the system and is therefore considered a fingerprint for the latter. Moreover, the peak at 600 cm^{-1} has been shown to be activated by the presence of aliovalent dopants, as is our case, with the addition of Gd^{3+}, and was hypothesized to originate from the F_1u (LO) phonon mode, usually only IR active, becoming Raman active due to the local lattice distortion relaxing symmetry rules[9]. This allow us to confirm the presence of oxygen vacancies in the system, as would be expected through the incorporation of aliovalent dopants such as Gd according to the following defect chemical reaction:

$$Gd_2O_{3_{CeO_2}} \rightarrow 2Gd'_{Ce} + V_{\ddot{O}} + 3O_O^x \quad \text{(S6)}$$

***Table** S1 Details of sample name, thickness and active area*

Name	Thickness	Active Area	Electrode
A	800-micron	5x9mm	yes
B	1mm	5x5mm	no
C	1mm	5x5mm	no

Figure S5 *Image of Sample A connected to in-situ measurement setup with 5x9 mm Pt Electrode on the front side.*

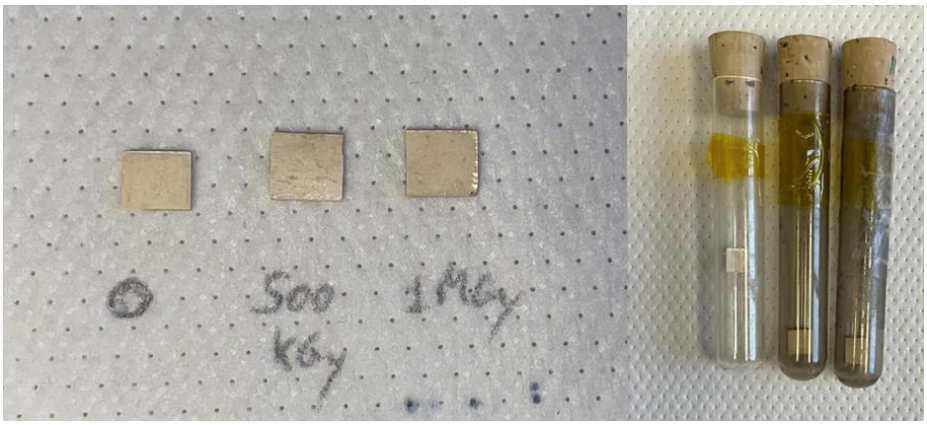

***Figure** S6 a) Example images of samples B that was split into three equal 5x5x1 cm samples and exposed to γ irradiation, b) Samples from series B inside their quartz test tube used for the irradiation experiment in order from left to right of increasing irradiation dose. Note the discoloration and increasing opacity of the test tube with irradiation dose, confirming the exposure of specimen to irradiation.*

IV. Additional Radiation Stability Data (XRD)

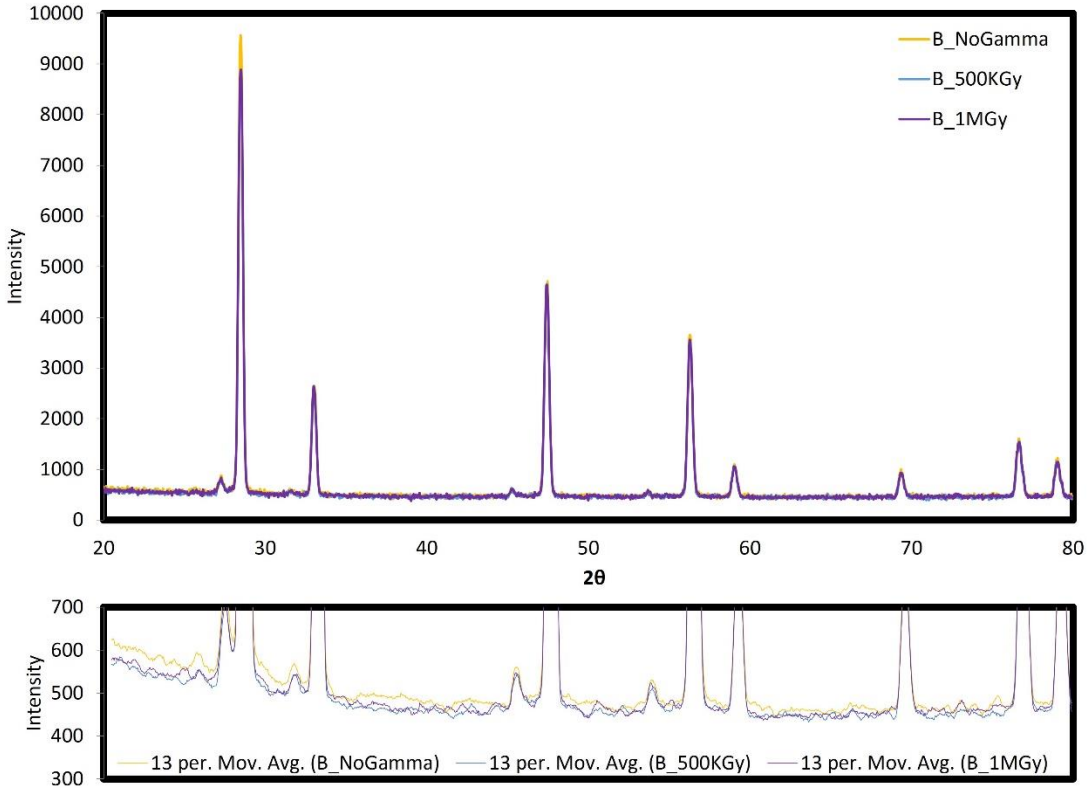

Figure S7 *(Top) Unnormalized and superimposed XRD spectra displayed in cascade in* ***Figure*** *4 for bulk samples of 3GDC series B, each exposed to various irradiation doses (0, 500 KGy, 1 MGy). (Bottom) Magnification of the 13-point averaged background for each sample, showing very little change in magnitude and shape.*

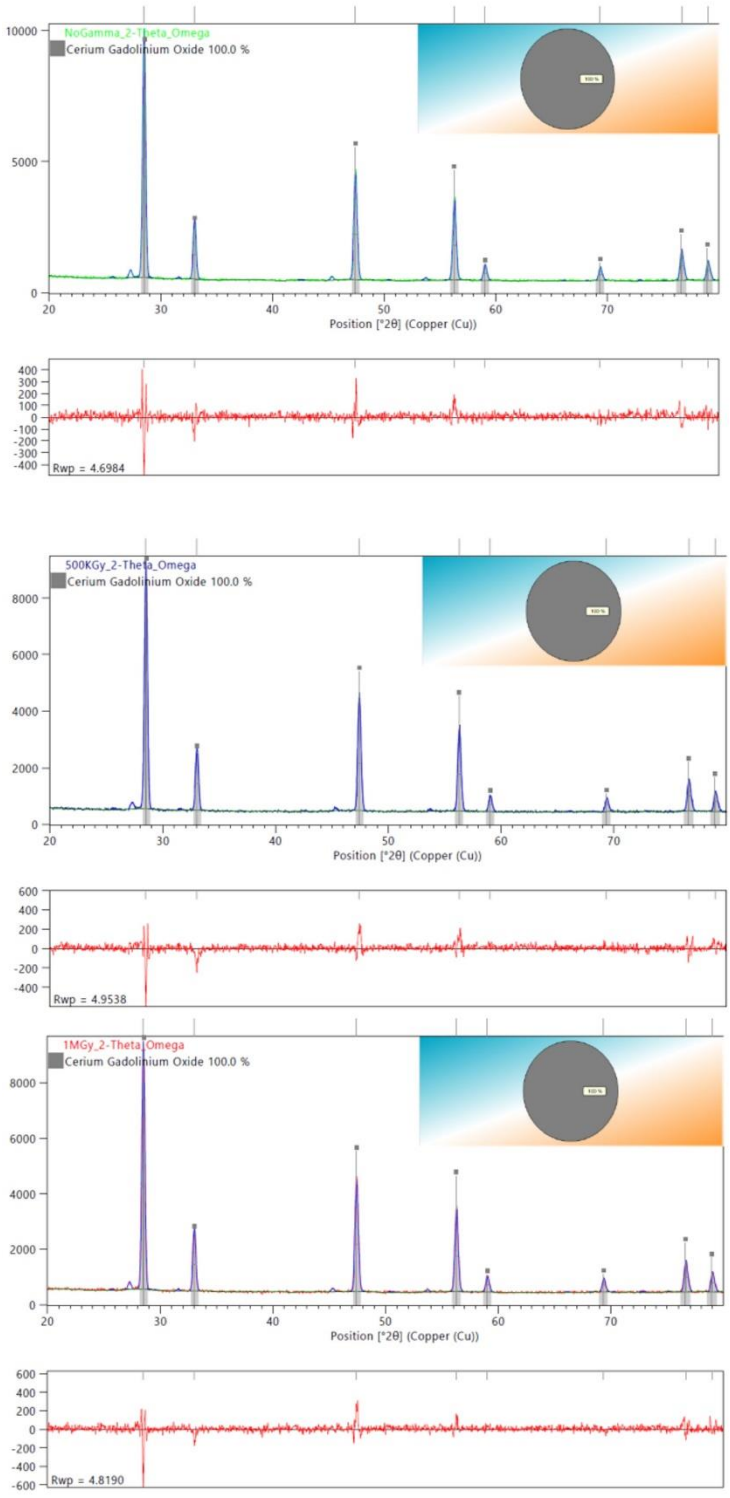

Figure S8 *Rietveld fitting method for sample B series: unirradiated GDC crystal structure (green), irradiated GDC structure at 500 KGy (blue) and irradiated GDC structure at 1 MGy (red).*

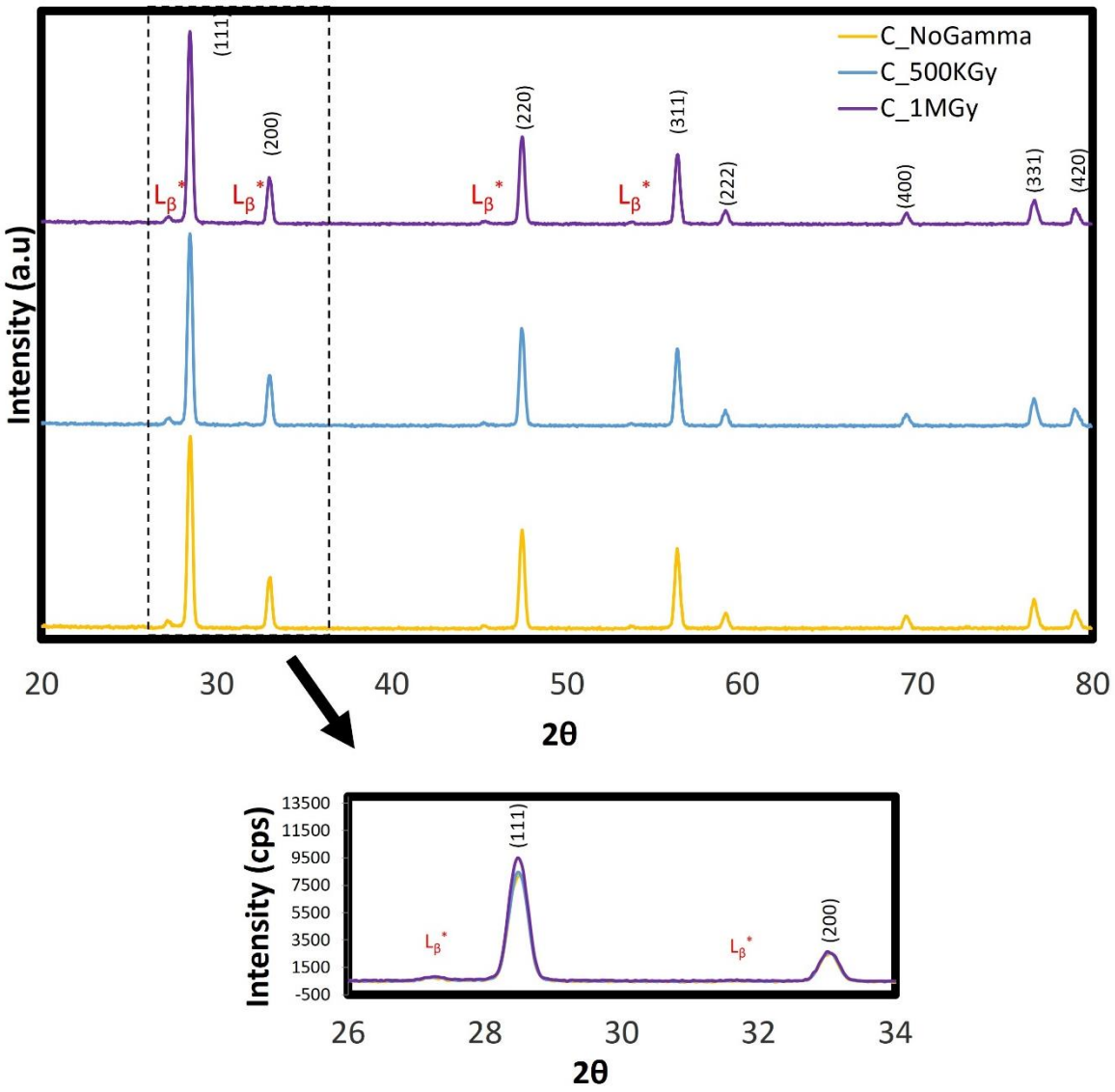

Figure S9 *(Top) Normalized and Cascaded XRD spectra for bulk samples of 3GDC series C, each exposed to various irradiation doses (0, 500 KGy, 1 MGy). (Bottom) Un-normalized magnification of superimposed (111) and (200) peaks for all three samples.*

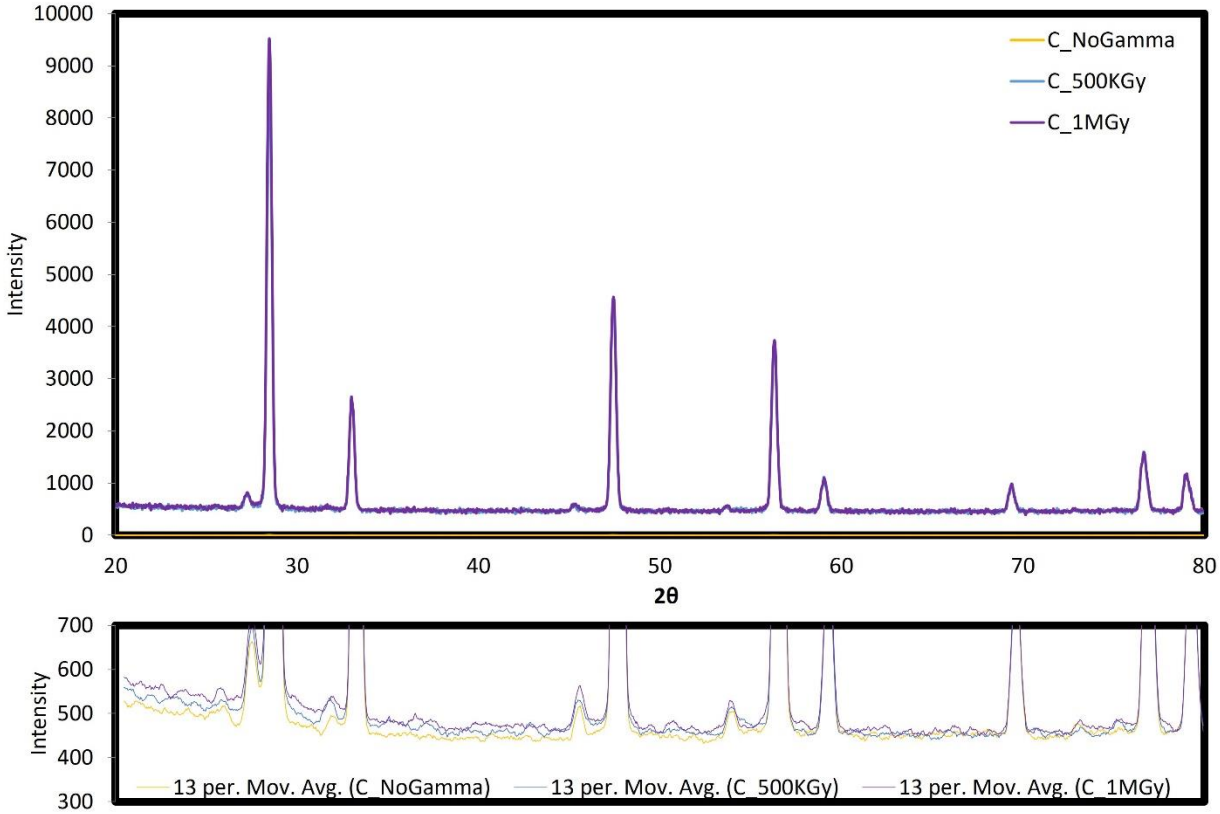

Figure S10 *(Top) Unnormalized and superimposed XRD spectra displayed in cascade in* ***Figure*** *S9 for bulk samples of 3GDC (C) each exposed to various irradiation doses (0, 500 KGy, 1 MGy). (Bottom) Magnification of the 13-point averaged background for each sample, showing very little change in magnitude and shape.*

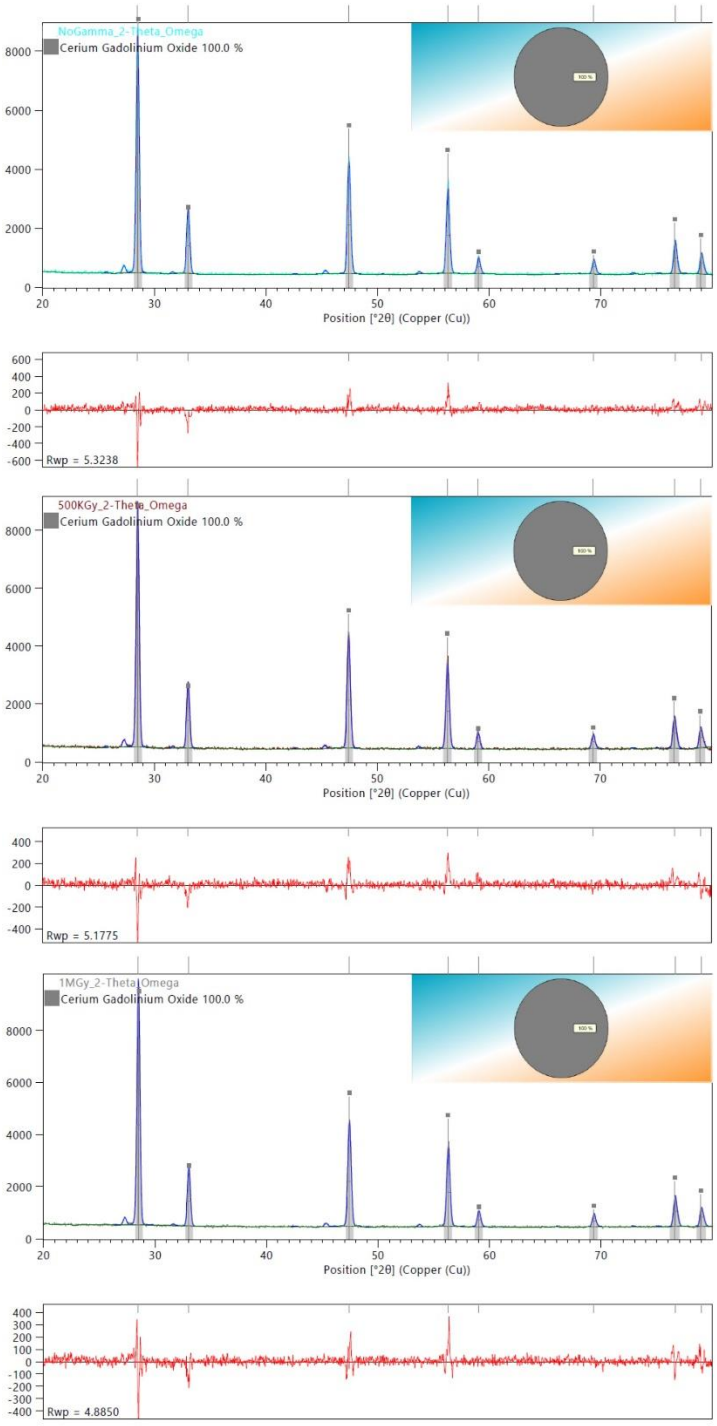

Figure S11 *Rietveld fitting method for sample C series: unirradiated GDC crystal structure (blue), irradiated 3GDC structure at 500 KGy (red) and irradiated GDC structure at 1 MGy (grey).*

Table S2. *Structural parameters for 3GDC sample C series for various γ irradiation conditions.*

Parameters	0 KGy	500 KGy	1000 KGy
Lattice Constants Å, a = b = c	5.412	5.412	5.412
Volume $(Å)^3$	158.516	158.516	158.516
March/Dollase (Preferred orientation)	0.89	0.90	0.80
Occupancy			
Ce	0.970	0.970	0.970
Gd	0.0292	0.0297	0.0298

V. Correcting for Porosity

Since the sample is not 100% dense, we need to correct the resistance and capacitance values obtained from the impedance spectra. This can be done using the Bruggeman symmetric model for 3–3 connectivity of spherical grains and pores (assuming the latter to have zero conductivity)

$$R_{corrected=}R_{porous}\left(1-\frac{3}{2}f\right) \qquad (S7)$$

where f is the volume fraction of pores. Other porosity correction models can also be considered, e.g. the Bruggeman asymmetric model[10,11] and Archie's model[11]. However, these do not result in significant differences versus the Bruggeman symmetric model employed. Furthermore, Perry et al[12] demonstrated good agreement between similarly porosity-corrected data for porous nano-YSZ and dense spark plasma-sintered YSZ specimens of comparable grain size. The porosity corrected capacitance can then be determined by assuming that the time constant (RC) of each arc remains unchanged by the correction:

$$R_{corrected}C_{corrected} = R_{porous}C_{porous} \qquad (S8)$$

VI. Heater Stick Temperature Calibration

We calibrated the temperature scale on our heater stick device by characterizing the dark conductivity of the same sample that was characterized in a tubular furnace, as displayed in **Figure** 3 of the main manuscript. Considering the small heating volume of the heater stick chip relative to

the pellet, this step was important to determine the actual temperature of the sample supported on the heater stick.

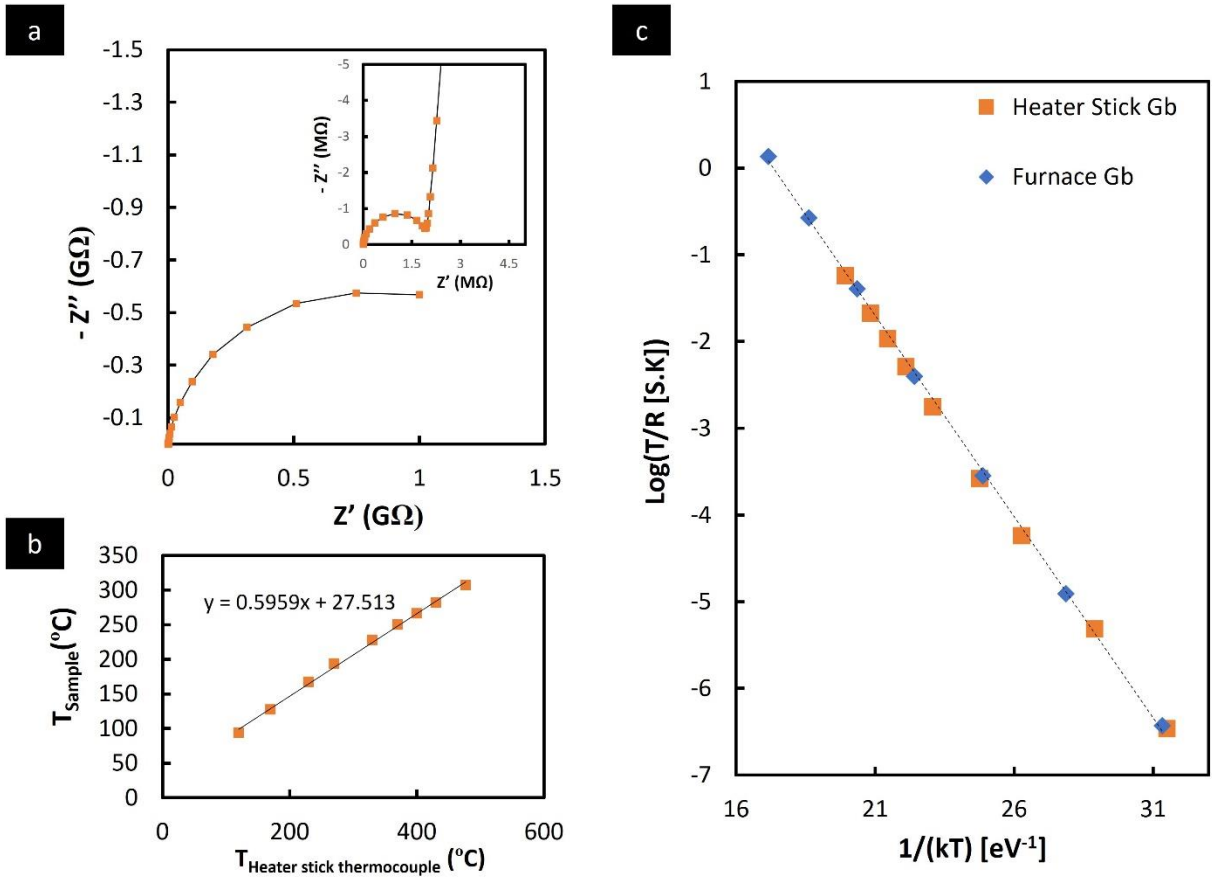

Figure S12 *Nyquist plot of the complex impedance response obtained under open-circuit conditions for the 3GDC pellet measured while supported on a heater stick in the dark, with inset showing the high frequency arc, b) temperature correspondence between the heater stick thermocouple temperature and the actual sample temperature, as calculated from the high frequency arc, and correlated with the furnace measurements, c) Plot of the Arrhenius dependence of the conductance x T vs. 1/kT for the low frequency arc (grain boundary contribution) for both the furnace and the heater stick measurements.*

As seen in **Figure** S12a, two semicircles were once again obtained. These impedance spectra match well with our observations in **Figure** 4a and by fitting with the same equivalent circuit, we obtain capacitance values (high frequency: 2.6×10^{-11} F, low frequency: 4.5×10^{-9} F respectively) allowing us to perform a similar assignment of bulk (high frequency) and grain boundary (low frequency) contributions. To calibrate the effective temperature of the samples, we cross-referenced the bulk resistance values obtained on the heater stick with those measured in the furnace, allowing us to calculate the true temperature of the sample (see **Figure** S12b). To verify the validity of this cross-referencing, we then plotted the grain boundary resistance values as a function of the effective temperature with those obtained in the furnace. As displayed in **Figure** S12c, one can see that the grain boundary values and the effective temperatures calculated by

cross-referencing the bulk resistance value, match well with the grain boundary values obtained for the specimen heated within the furnace, confirming the adequacy of the calibration protocol.

VII. High Frequency Close-up of Nyquist plot

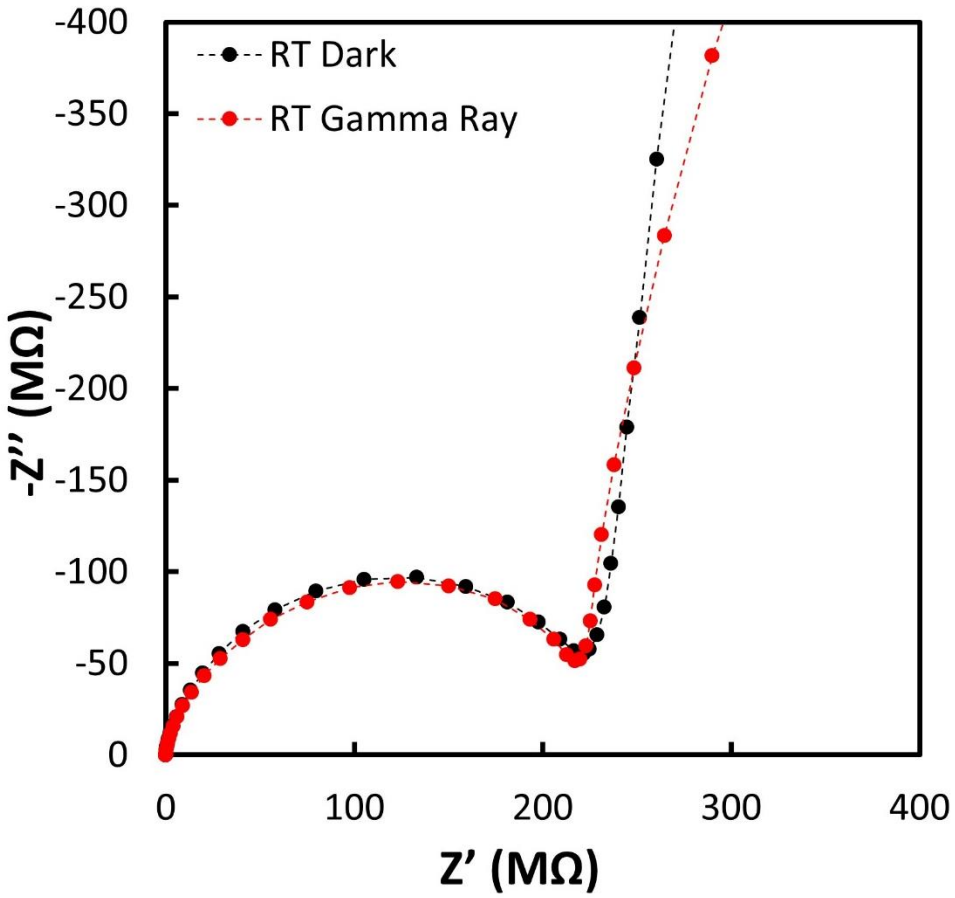

Figure S13 *High Frequency close-up of Nyquist plots of the complex impedance response obtained under open-circuit conditions for the 3GDC pellet measured at 23.8℃ in the dark and under gamma irradiation (Dark vs Gamma Ray). This displays how the bulk impedance changes only very slightly under irradiation.*

VIII. Reproducibility and Reversibility

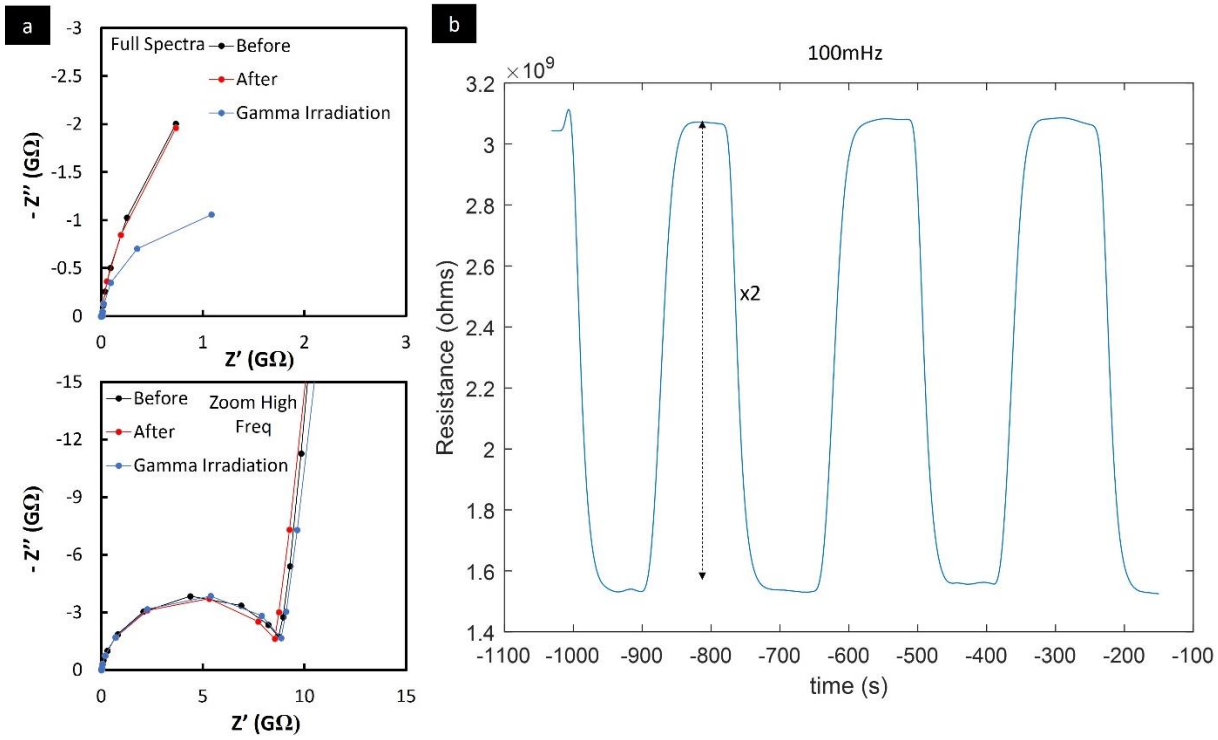

Figure S14 a) *Before-during-and-after gamma irradiation impedance cycles measured at 67ºC. The same Gammacell 220 was used to irradiate the sample, however the irradiation dose was equal to ~20 Grey/min. b) Three cycles of single-frequency relaxation, captured at 100 mHz, where the total impedance of the system is measured at a single frequency over time as the sample is cycled in and out of the gamma ray irradiator under similar irradiation conditions.*

In **Figure S14a** we display the impedance of the sample measured at 67ºC (before-during-and-after exposing it to ~20 Grey/min Gamma irradiation). We summarize the fitting and porosity corrected results in **Table S3**. As shown in the impedance spectra in **Figure S14a**, the high frequency semi-circle, associated with bulk transport remains predominantly unchanged (small 2% change), before and after gamma irradiation, while the lower frequency impedance associated with grain boundary resistance is depressed by 240% under irradiation and returns to its dark value upon removal from the radiation source within a variance of 4%. The small changes in the bulk and grain boundary data upon return to dark conditions have been associated with the low accuracy of the manual temperature control. As can be seen in **Figure S14b**, the single frequency measurements over time show that the total electrical response is fully reversible as we cycle the sample in and out of the radiator. The frequency is selected based on the impedance such that it captures part of the resistance of the grain boundary, while also remaining experimentally

accessible (measurement duration for frequencies below 100 mHz is so slow that it can lead to errors given the manual temperature control).

***Table** S3- Summary of the Impedance fit results (Resistance & Capacitance) of the spectra's presented in Figure S14a, corrected for porosity.*

		Bulk		Grain Boundary	
		Resistance (Mohms)	Capacitance (pF)	Resistance (Gohms)	Capacitance (nF)
	before	7.79	10.2	6.79	4.92
	After	7.63	9.54	6.56	4.95
	Gamma	7.94	9.48	1.98	4.35
Before/Under Irradiation	ratio of Conductances	0.98		3.42	
	percentage change	2%		-243%	
Before/After Irradiation	ratio of Conductances	1.02		1.04	
	percentage change	-2%		-4%	

We note that in terms of response time, based on the single frequency relaxation curves added to the manuscript, these devices take several 10's of seconds to reach steady state under irradiation at 67ºC. This is consistent, as previously established in our paper on optical illumination of thin films[4]. As established previously, the response rate of the optoionic response is controlled by the rate of anion diffusion in and out the space charge region. By using values of the bulk ionic diffusivity (D_o) in 3 atm% Gd doped CeO_2, that depends on the vacancy diffusivity $D_o \approx n_v D_v$ multiplied by the site fraction of oxygen vacancies to oxygen ions in the lattice $n_v = \frac{[V]}{[O]}$ - see literature[13], we calculate a diffusion time $\tau = \frac{x^2}{D_o}$ within the length of a space charge width (~1-2 nm). From these values, we obtain a diffusion coefficient equal to $1.25*10^{-14}$ to $5.33*10^{-14}$cm^2/s at 50-70ºC, that leads to expected diffusion times of 9 to 40 s. These time scales align with our single frequency relaxation data obtained at 67ºC. As we discuss in the manuscript, alternative ion conducting material systems, with faster bulk ionic mobilities, such as Li^+ or OH^+, can be expected to achieve orders of magnitude faster response times. This could, in turn, be more enabling for certain technologies such as spectroscopy. These studies are part of our ongoing effort to develop the fundamental science and benchmark performance metrics for this new ionic conductive materials category.

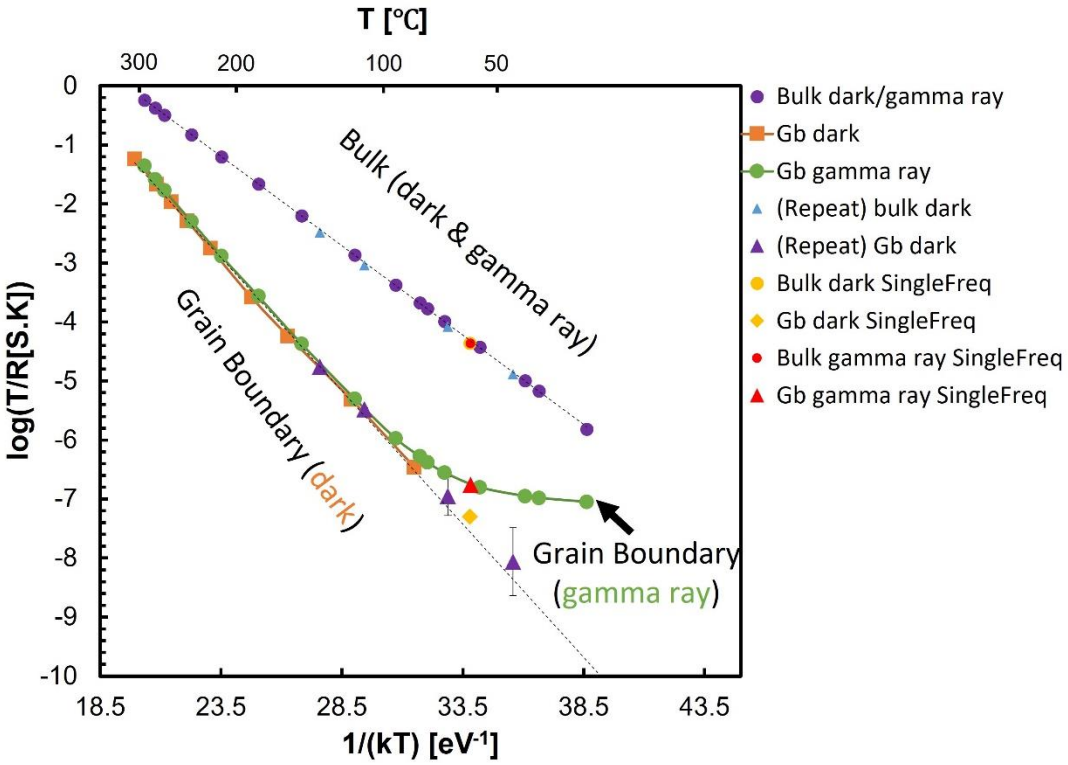

Figure *S15 Plot of the Arrhenius dependence of the logarithm of the conductance (1/R) × T vs. $1/k_BT$ corresponding to the high frequency and low-frequency arcs (related to grain and grain boundary contributions, respectively) obtained in the dark and under irradiation. Additional repeat measurements are provided. Repeat Gb Dark values down to lower temperatures show that our high temperature extrapolation of the grain boundary resistance down to room temperature is valid, within fitting error. Gb and Bulk Gamma ray single frequency results show that our measurements in* ***Figure*** *S14 are consistent with our previous measurements displayed in Figure 4.*

IX. Constriction Model

We refer the readers to more a detailed explanation in the supplementary of article[4] with additional schematics to help visualize the model. This simplified model aids in understanding the unusual temperature dependence of the measured resistance of a polycrystalline solid electrolyte under steady state irradiation conditions. We summarize here the key elements to explain how the calculation of the 10 % constriction area at room temperature was derived in the discussion section of the main article.

Considering the naturally expected distribution of space charge potentials that exist at grain boundaries in polycrystalline oxides, and the fact that for a given light intensity only fraction of barriers (starting with the smallest barrier) can be fully collapsed, then the current pathway through the material can be modelled as a percolating pathway. This observation arises from the fact that the resistance of grain boundaries whose space charge potential have not collapsed will be high, especially at lower temperatures (due to the higher activation energy), and that the current will prefer to flow through the grain contact points with a space charge potential that collapsed to zero under irradiation. In that scenario, current flow will possess a resistance $R_{\mathrm{gb,tot}}^{(//)}$ with a bulk-like behavior, but only represent a fraction of the total film volume that can be described as follows (Eq. S9 is the same as Eq. 3 in the main manuscript):

$$\frac{R_{\mathrm{gb,tot}}^{(//)}}{R_{\mathrm{bulk,tot}}} = f_{\mathrm{path}} \qquad (S9)$$

where we define f_{path} as a lumped geometrical factor accounting for the decreased conductive area (as compared to the sample's full conductive area) and the tortuosity, the elongation of the pathway. The whole system can then be described as two parallel resistances, where the measured resistance $R'_{\mathrm{gb,tot}}$ is given by

$$\frac{1}{R'_{\mathrm{gb,tot}}} = \frac{1}{R_{\mathrm{gb,tot}}(T)} + \frac{1}{R_{\mathrm{gb,tot}}^{(//)}(T)} \qquad (S10)$$

where the main parameter being impacted by light is the factor f_{path} and reaches a maximum value of 1 when all the grain boundaries become non-blocking (space charge potential of zero).

X. Mean Penetration Depth

The program "XCOM" (NIST XCOM: Element/Compound/Mixture) can be used to calculate the attenuation coefficients for undoped CeO_2 as a first approximation. This information is also useful in order to determine whether the incident radiation interacts with the entirety of the sample volume. **Figure** S16 shows plots of total mass attenuation coefficients (a) and mean penetration (b) as a function of photon energy. At a photon energy of 1 MeV, the mean penetration in CeO_2 is approximately 1cm.

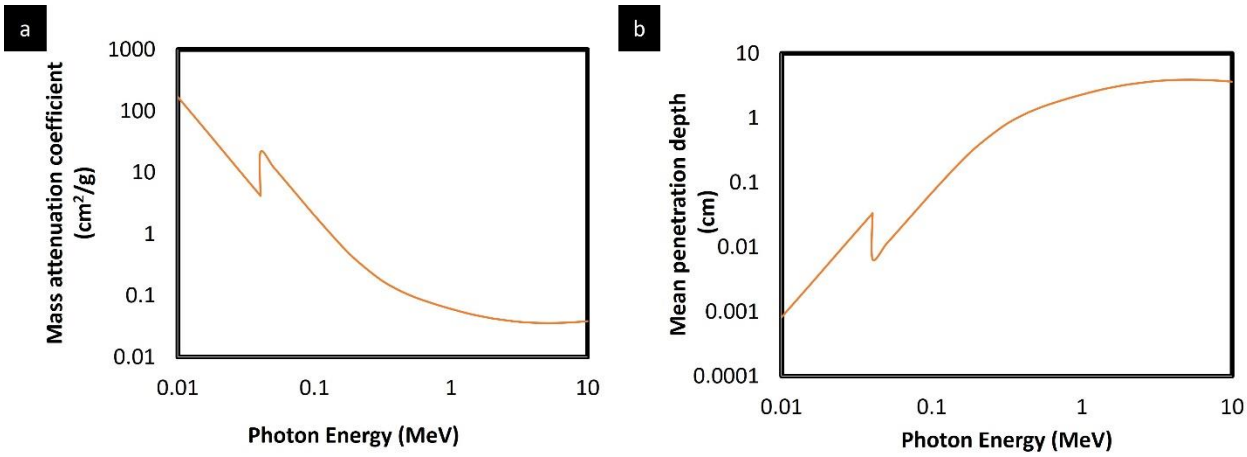

Figure S16 *(a) Predicted Mass attenuation coefficient for CeO_2 and (b) Mean penetration depth of High Energy Gamma Rays (0.01- 10 MeV)*

XI. Temperature Dependance of f_{path}

To understand the temperature dependence of the opto-ionic effect referred to here, we need to consider the physics that relates to the charge trapping kinetics at grain boundaries in semiconductors under illumination, previously derived by Seager et. al. and others in the case of silicon. While those are advanced models derived from first principal rate theory, to discuss the generally expected temperature dependence, we refer to a review by Grovenor, et al[14] who discusses the key equations derived by Seager, et al.[15,16]. Generally, illumination of a polycrystalline semiconductor will produce a non-equilibrium distribution of both majority and minority electronic carriers near the grain boundaries. The minority electronic n type carriers (see **Figure** S1 above) will drift rapidly towards the boundaries due to the field gradient in the space-charge regions. This flux of minority carriers to the boundary and their subsequent trapping into the interface states, will lower the net charge on the boundary. This in turn will reduce the grain boundary space charge potential and surrounding band-bending. A steady state condition will be reached when the flux of minority carriers down the now reduced potential gradient is balanced by a flux of majority carriers to the interface states. This condition can be stated under zero applied bias more formally as:

$$2qD_n\frac{dn}{dx} = 2cAexp\left(\frac{\Delta\varphi(0)}{kT}\right) \qquad (S11)$$

where D_n is the minority carrier diffusion coefficient, n the concentration of minority electronic carriers, c parameter describing the majority (electronic) carrier capture rate at grain boundaries, A the pseudo-Richardson coefficient. The equilibrium recombination velocity is then defined as:

$$S = \frac{1}{q}v_{th}\sigma_n\left(2\varepsilon\varepsilon_0 N_t\Delta\varphi(0)\right)^{0.5}\,exp\left(\frac{\Delta\varphi(0)}{kT}\right) \qquad (S12)$$

Where v_{th} is the thermal velocity of minority electronic carrier, σ_n capture cross-section of a filled interface state for a minority carrier and N_t the density of interface trap states. The recombination

velocity, is key to understanding the physics of charge carrier trapping at the interface and is fundamentally split between 1) the extent that the space charge fields can split and collect the photogenerated charges and 2) on the ability of the core grain boundary traps to maintain the trapped charges, reflected by the capture cross section of the trap states at the grain boundary and the thermal velocity of the minority charge carriers.

When considering its overall temperature dependence, we can inspect equation (S12) and observe that a natural temperature dependence exists as an exponential term which relates to the temperature dependent weakening of the field lines in the space charge zone (i.e. $exp\left(\frac{\Delta\varphi(0)}{kT}\right)$). Moreover, another important term in this equation, also expected to exhibit a strong temperature dependence is σ_n, the minority carrier captures cross section. Although the temperature dependence of charge carrier recombination for our material system has never, to the best of our knowledge, been measured, we can consider other materials systems and experimentally measured recombination lifetime temperature dependencies for comparison. For example, p-type polycrystalline silicon, an indirect band gap semiconductor exhibits very similar space charge properties as the case of ceria (positively charged grain boundary core). Reports in the literature[17] have shown that contrary to single crystalline silicon that exhibits a direct band recombination process with a negative temperature dependence of the carrier lifetimes, in the case of polycrystalline silicon, defects at grain boundaries control the recombination process, and this can lead to a positive thermally activated temperature dependence. This positive thermally activated temperature dependence of the minority carrier lifetime at grain boundaries is associated with the capture cross section obeying a *Cascade Phonon Capture* mechanism, typical for Coulomb attraction centers, such as shallow impurities or charge defect states [18,19]. The general temperature dependence of the capture cross sections be expressed as an Arrhenius equation according to[19,20]:

$$\sigma_n\,(E_t, T) = \sigma_0\,(E_t)\exp\left(-\frac{\Delta E_\sigma(E_t)}{kT}\right) \qquad (S13)$$

Where $\sigma_0\,(E_t)$ reflects the fact that capture cross section of a defect posses' inherent properties that depend on the type of defect and the energy depth of that level with respect to the conductance band edge, E_t. $\Delta E_\sigma(E_t)$, also depends on the type of defect, but predominantly depends on the depth of the energy levels and its relative position to the Fermi level (i.e $\Delta E_\sigma(E_t) \sim (E_t - E_F)$) and is representative of the main mechanism controlling the population density of trapped carriers, which is a thermalization step instead of direct recombination. In the case of the Cascade phonon recombination mechanism, the value of $\Delta E_\sigma(E_t)$ can be negative [19,21] indicative of the fact that at higher temperatures the capture cross section becomes smaller. This reflects the fact that there is a certain probability of the trapped defect thermalizing due to the absorption of phonons which can depopulate the trapped states before recombination occurs (i.e., the population density of trapped charge carrier is controlled by their thermalization rate to the conduction band).

Combining those two facts: temperature dependence of space charge field, which would scale with the space charge potential ($\Delta\phi(0) \sim 0.2\ eV$), and the capture cross section, which would scale with the energy of the trap state in the band bap ($\Delta E_\sigma(E_t)$), one would therefore expect a rather large negative exponential dependence on temperature for the grain boundary recombination kinetics leading to a similar temperature dependence of the f_{path} parameter. Depending on the value of $\Delta E_\sigma(E_t)$, the activation energy of f_{path} could indeed reach similar magnitudes, but opposite in sign, to that of bulk ionic conduction, and therefore lead to a nearly flat overall temperature

dependence as observed. Future studies examining the temperature dependence of the photo-generated minority charge carrier lifetime, energy levels of traps states at the interfaces and the recombination velocity at the grain boundaries will be necessary to confirm such a hypothesis.

XII. References

1. Guo, X. & Waser, R. Electrical Properties of the Grain Boundaries of Oxygen Ion Conductors: Acceptor-doped Zirconia and Ceria. Prog Mater Sci 51, 151–210 (2006).

2. Gregori, G., Merkle, R. & Maier, J. Ion Conduction and Redistribution at Grain Boundaries in Oxide Systems. Prog Mater Sci 89, 252–305 (2017).

3. Tong, X., Mebane, D. S. & De Souza, R. A. Analyzing the Grain Boundary Resistance of Oxide Ion Conducting Electrolytes: Poisson-Cahn vs Poisson-Boltzmann theories. Journal of the American Ceramic Society 103, 5–22 (2020).

4. Defferriere, T., Klotz, D., Gonzalez-Rosillo, J. C., Rupp, J. L. M. & Tuller, H. L. Photo-enhanced Ionic Conductivity Across Grain Boundaries in Polycrystalline Ceramics. Nat Mater 21, 438–444 (2022).

5. Usler, A. L. & De Souza, R. A. A Critical Examination of the Mott–Schottky Model of Grain-Boundary Space-Charge Layers in Oxide-Ion Conductors. J Electrochem Soc 168, 056504 (2021).

6. Xu, X., Liu, Y., Wang, J., Isheim, D., Dravid, V. P., Phatak, C. & Haile, S. M. Variability and Origins of Grain Boundary Electric Potential Detected by Electron Holography and Atom-Probe Tomography. Nat Mater 19, 887–893 (2020).

7. Rabbani, A. & Salehi, S. Dynamic Modeling of the Formation Damage and Mud Cake Deposition Using Filtration Theories Coupled with SEM Image Processing. J Nat Gas Sci Eng 42, 157–168 (2017).

8. Ezeakacha, C. P., Rabbani, A., Salehi, S. & Ghalambor, A. Integrated Image Processing and Computational Techniques to Characterize Formation Damage. in Proceedings - SPE International Symposium on Formation Damage Control 2018-February, (OnePetro, 2018).

9. Schmitt, R., Nenning, A., Kraynis, O., Korobko, R., Frenkel, A. I., Lubomirsky, I., Haile, S. M. & Rupp, J. L. M. A Review of Defect Structure and Chemistry in Ceria and its Solid Solutions. Chem Soc Rev 49, 554–592 (2020).

10. McLachlan, D. S., Blaszkiewicz, M. & Newnham, R. E. Electrical Resistivity of Composites. Journal of the American Ceramic Society 73, 2187–2203 (1990).

11. Archie, G. E. The Electrical Resistivity Log as an Aid in Determining Some Reservoir Characteristics. SPE Reprint Series 9–16 (2003).

12. Perry, N. H., Kim, S. & Mason, T. O. Local Electrical and Dielectric Properties of Nanocrystalline Yttria-Stabilized Zirconia. J Mater Sci 43, 4684–4692 (2008).

13. Waldow, S. P. & De Souza, R. A. Is Excess Faster Than Deficient? A Molecular-Dynamics Study of Oxygen-Interstitial and Oxygen-Vacancy Diffusion in CeO_2. Journal of Physics: Energy 2, 024001 (2020).

14. Grovenor, C. R. M. Grain Boundaries in Semiconductors. J. Phys. C: Solid State Phys 18, 4079–4119 (1985).

15. Seager, C. H. Grain Boundary Recombination: Theory and Experiment in Silicon. J Appl Phys 52, 3960–3968 (1981).

16. Seager, C. H. Temperature Dependence of Minority-Carrier Recombination Velocities at Grain Boundaries in Silicon. Appl Phys Lett 41, 855–857 (1982).

17. Mathur, P. C., Sharma, R. P., Saxena, P. & Arora, J. D. Temperature Dependence of Minority-Carrier Lifetime in Single-Crystal and Polycrystalline Si Solar Cells. J Appl Phys 52, 3651–3654 (1981).

18. Bourgoin, J. C. Multiphonon Capture in the Case of Undistorted Defects. Phys Rev B 38, (1988).

19. Bourgoin, J. & Lannoo, M. in Point Defects in Semiconductors II Experimental Aspects (1983).

20. Katsube, T., Kakimoto, K. & Ikoma, T. Temperature and Energy Dependences of Capture Cross Sections at Surface States in Si Metal-Oxide-Semiconductor Diodes Measured by Deep Level Transient Spectroscopy. J Appl Phys 52, 3504–3508 (1981).

21. Lax, M. Cascade Capture of Electrons in Solids. Physical Review 119, 1502–1523 (1960).